AGU
ADVANCING EARTH AND SPACE SCIENCE

JGR Oceans

Key Points:

- Submarine melt and subglacial discharge follow theoretical scaling (melt ~ discharge$^{1/3}$), but the magnitude of melt is much larger than theory
- Subglacial discharge has a stronger influence on submarine melt than fjord conditions, because discharge varies by 2+ orders of magnitude
- Submarine melt removes up to ~50% of the ice flux into the terminus and is correlated with terminus retreat in summer

Supporting Information:

Supporting Information may be found in the online version of this article.

Correspondence to:

R. H. Jackson,
rjackson@marine.rutgers.edu

The Relationship Between Submarine Melt and Subglacial Discharge From Observations at a Tidewater Glacier

Rebecca H. Jackson[1] , Roman J. Motyka[2,3], Jason M. Amundson[3] , Nicole Abib[4], David A. Sutherland[4] , Jonathan D. Nash[5] , and Christian Kienholz[3]

[1]Department of Marine & Coastal Sciences, Rutgers University, New Brunswick, NJ, USA, [2]Geophysical Institute, University of Alaska Fairbanks, Fairbanks, AK, USA, [3]Department of Natural Sciences, University of Alaska Southeast, Juneau, AK, USA, [4]Department of Earth Sciences, University of Oregon, Eugene, OR, USA, [5]College of Earth, Ocean & Atmosphere Sciences, Oregon State University, Corvallis, OR, USA

Abstract At tidewater glacier termini, ocean-glacier interactions hinge on two sources of freshwater—submarine melt and subglacial discharge—yet these freshwater fluxes are often unconstrained in their magnitude, seasonality, and relationship. With measurements of ocean velocity, temperature and salinity, fjord budgets can be evaluated to partition the freshwater flux into submarine melt and subglacial discharge. We apply these methods to calculate the freshwater fluxes at LeConte Glacier, Alaska, across a wide range of oceanic and atmospheric conditions during six surveys in 2016–2018. We compare these ocean-derived fluxes with an estimate of subglacial discharge from a surface mass balance model and with estimates of submarine melt from multibeam sonar and autonomous kayaks, finding relatively good agreement between these independent estimates. Across spring, summer, and fall, the relationship between subglacial discharge and submarine melt follows a scaling law predicted by standard theory (melt ~ discharge$^{1/3}$), although the total magnitude of melt is an order of magnitude larger than theoretical estimates. Subglacial discharge is the dominant driver of variability in melt, while the dependence of melt on fjord properties is not discernible. A comparison of oceanic budgets with glacier records indicates that submarine melt removes 33%–49% of the ice flux into the terminus across spring, summer, and fall periods. Thus, melt is a significant component of the glacier's mass balance, and we find that melt correlates with seasonal retreat; however, melt does not appear to directly amplify calving.

Plain Language Summary Two main sources of freshwater enter the ocean at the fronts of tidewater glaciers: submarine melt and subglacial discharge. Submarine melt is thought to play a role in triggering ice loss at glaciers around the globe. Submarine melt, in turn, is modulated by subglacial discharge and fjord conditions. However, we have few direct measurements of submarine melt and subglacial discharge at tidewater glaciers. Instead, many studies rely on theory to predict melt rates as a function of modeled subglacial discharge and fjord conditions. In this study, we use measurements of ocean velocity and water properties to estimate the fluxes of submarine melt and subglacial discharge from LeConte Glacier, Alaska. We find that melt varies as a function of discharge in the manner predicted by theory, but the overall magnitude of melt is substantially higher than theory. The impact of fjord temperature and stratification on melt is secondary and does not form a clear signal in the data. Overall, submarine melt removes approximately half of the ice flux into the terminus and is correlated with terminus retreat in summer. However, there is no clear relationship between melt and calving, suggesting that submarine melt does not directly amplify calving on seasonal timescales.

1. Introduction

Two main types of freshwater enter the ocean at the termini of tidewater glaciers: submarine melt from ice that melts directly into the ocean, and subglacial discharge from surface melt or precipitation that drains to the bed of the glacier and then into the ocean. These freshwater sources form plumes that rise along the submarine terminus, driving mixing between glacial freshwater and seawater. The dynamics of these plumes affect both submarine melt rates and fjord circulation (e.g., Carroll et al., 2015; Jenkins, 2011). Subglacial discharge, in particular, plays a dual role in forcing both the ocean and glacier: it is often the largest source of freshwater into fjords, driving a strong buoyancy-driven circulation, and also modulates submarine melt rates by altering the turbulent transfers at the ice-ocean boundary (Holland & Jenkins, 1999; Sciascia et al., 2013; Slater et al., 2015). Submarine melt,

in turn, likely plays a role in triggering glacier acceleration, thinning, and retreat, particularly for glaciers with floating tongues (Motyka et al., 2011; Nick et al., 2009; Straneo & Heimbach, 2013; Wood et al., 2018).

Despite the importance of these freshwater inputs for ocean-glacier interactions, the fluxes of submarine melt and subglacial discharge are poorly constrained with observations. Subglacial discharge is often estimated from surface mass balance (SMB) models of runoff over a glacier's catchment basin (e.g., Hock, 2005). Such models, however, have not been validated at marine-terminating glaciers since there is currently no way of directly measuring subglacial discharge as it enters the ocean. For submarine melt, a variety of methods have been developed to measure melt rates at the base of floating ice shelves and ice tongues (e.g., Jenkins et al., 2010; Wilson et al., 2017), but such methods have not been feasible at tidewater glaciers where the termini are near-vertical, actively calving, and typically grounded. With the exception of Sutherland et al. (2019), who used repeat sonar imaging to track the terminus evolution, direct measurements of submarine melt rates at tidewater glaciers have been lacking.

While direct measurements of subglacial discharge and submarine melt are limited, indirect estimates of both freshwater types can be derived from oceanic measurements of velocity, temperature, and salinity in fjords downstream of glaciers (Jackson & Straneo, 2016; Motyka et al., 2003). While many studies have used some variation of this "fjord budgets" approach (e.g., Inall et al., 2014; Motyka et al., 2013; Xu et al., 2013), previous results have been limited by: measurements made only in summer; significant gaps in the spatial coverage or temporal resolution of the observations; measurements often collected far from the glacier; and/or inconsistencies in methods and equations—all of which result in large uncertainties and limitations in the scope of the previous results. Furthermore, these estimates of submarine melt and subglacial discharge from fjord budgets have not been thoroughly compared against other independent estimates, such as SMB models.

In the absence of robust observations of submarine melt, theory and models are typically used to predict melt rates as a function of ocean conditions and subglacial discharge (with subglacial discharge, in turn, estimated from an SMB model). In the most common application, buoyant plume theory is used to represent the upwelling plumes of subglacial discharge and/or submarine meltwater as they rise along the terminus, while a melt parameterization calculates the submarine melt rate based on the near-glacier velocity, temperature, and salinity (Jenkins, 2011; MacAyeal, 1985). When these two pieces are coupled together, hereafter referred to as "plume-melt theory," then melt rates can be derived based on inputs of subglacial discharge and fjord conditions. This is a widely used framework (e.g., Cowton et al., 2015; De Andrés et al., 2020; Mankoff et al., 2016, and many others) but largely untested with observations (Straneo & Cenedese, 2015).

Within this framework, there are two regimes of melting. First, discharge-driven melting exists where subglacial discharge plumes are in contact with the ice face. We expect high velocities in the rising plume, corresponding to elevated melt rates. Much of the literature has focused on this regime, and plume-melt theory predicts that total submarine melt, Q_M, will scale as: $Q_M \sim (\theta - \theta_f) Q_R^{1/3}$—a linear dependence on thermal forcing ($\theta - \theta_f$, potential temperature above freezing) and a 1/3 power-law dependence on subglacial discharge, Q_R (with some small variations in the exponent depending on the melt regime, Slater et al., 2016). Away from the discharge plume or plumes, ambient melt occurs where the ice melts directly into the ambient fjord waters. Velocities in this region are determined from a combination of vertical upwelling from meltwater convection (i.e., plumes of submarine meltwater) and other modes of fjord circulation (Magorrian & Wells, 2016; Slater et al., 2018). Standard plume-melt theory only accounts for the upwelling velocities and—when considered in isolation—suggests very weak plumes, low melt rates, and almost negligible ambient melt compared to discharge-driven melt (at least in summer) (Carroll et al., 2016; Cowton et al., 2015). This has led many studies to focus exclusively on the discharge-driven melting and to assume that, since discharge-driven melt is dominant, the total melt would also scale with $Q_R^{1/3}$ (e.g., Slater et al., 2019). Bulk parameterizations in this form, which predict melt as a function of forcing quantities, are critical for modeling ocean-glacier interactions, yet, to date, these bulk parameterizations have not been tested with observations across a range of forcing conditions.

Further motivating the need to test existing theory, several recent studies have indicated that plume-melt theory significantly underpredicts the magnitude of submarine melting. Sutherland et al. (2019) used multibeam sonar and radar to make direct estimates of the submarine melt rates at LeConte Glacier, finding melt rates of ~5 m d⁻¹ averaged over most of the terminus, which is one to two orders of magnitude larger than theory predicts. Additionally, kayak surveys within 400 m of LeConte terminus reveal ubiquitous meltwater intrusions from ambient
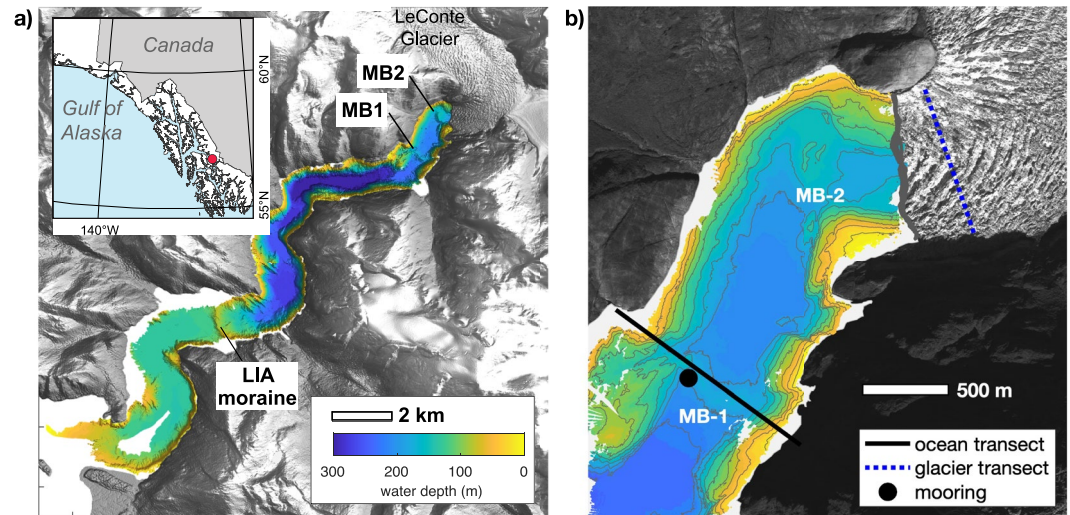
Figure 1. (a) LeConte Glacier and fjord bathymetry with the three sills within the fjord marked. Adapted from Eidam et al. (2020). (b) Zoom of near-glacier region with locations of the ocean transect for budget calculations and the glacier transect for ice flux measurements—for all surveys except September 2018—and the mooring location. Bathymetry is shown with the same colormap as in (a).

melting, indicating that ambient melt is a substantial part of the total terminus melt (Jackson et al., 2020). On its own, this result might suggest that net melting is less sensitive to subglacial discharge than standard plume-melt theory predicts. However, until this paper, there have not been simultaneous estimates of subglacial discharge, submarine melt, and fjord properties across a wide range of conditions to test the theoretical relationship between submarine melt and environmental drivers.

Here, we evaluate fjord budgets to estimate the fluxes of subglacial discharge and submarine melt at LeConte Glacier in six different field campaigns that span a wide range of oceanic conditions in spring, summer, and early fall. The driving questions for this work are two-fold: first, how well does the budgets method work to measure subglacial discharge and submarine melt fluxes? To do this, we will compare the budgets results with estimates of subglacial discharge from an SMB model and estimates of submarine melt from multibeam sonar and kayak surveying (Jackson et al., 2020; Sutherland et al., 2019). Second, how does submarine melt vary with subglacial discharge and fjord conditions? We examine this relationship between melt and its potential drivers across a wide parameter space to test the existing theory and to explore potential adjustments that might lead to a more accurate parameterization for submarine melt. Finally, we combine these primary results with glacier records to discuss the implications of submarine melt for glacier dynamics.

2. Setting and Data

2.1. LeConte Glacier and Fjord

LeConte Glacier (Xeitl Sít' in Tlingit) drains the Stikine Icefield into LeConte Bay (Xeitl Geeyi'). LeConte is the southernmost tidewater glacier in the northern hemisphere and has an annual ice flux of ∼1 Gt a^{-1} (McNabb et al., 2015). LeConte Bay is a narrow, sinuous fjord—between 1 and 2 km wide and 18 km long—with several deep subbasins separated by three morainal banks: MB1, MB2, and LIA (Little Ice Age) as shown in Figure 1 (Eidam et al., 2020; Motyka et al., 2003). The glacier currently terminates in water depths ranging from 170 to 200 m and undergoes seasonal advance/retreat oscillations of ∼300 m (Eidam et al., 2020).

At the terminus, one or two subglacial discharge plumes are observed flowing away from the glacier at or near the ocean surface (Kienholz et al., 2019; Motyka et al., 2003, 2013). In addition to the subglacial discharge plumes, submarine meltwater intrusions from ambient melt are ubiquitous within 400 m of the terminus (Jackson et al., 2020). A variety of independent observations—from multibeam sonar, autonomous kayak surveys, and downstream ocean fluxes—suggest submarine melt rates of 1–16 m d^{-1} (Jackson et al., 2020; Motyka et al., 2013; Sutherland et al., 2019). There is typically open water near the terminus, although occasionally ephemeral ice

Table 1
Variable definitions, values, and units

Symbol	Meaning	Value	Units
ρ	Density of seawater	1,027	kg m^{-3}
ρ_i	Density of ice	910	kg m^{-3}
c_p	Heat capacity of seawater	4,030	J kg^{-1}°C^{-1}
c_i	Heat capacity of ice	2,100	J kg^{-1}°C^{-1}
θ_M	Temperature of Q_M	−1.6	°C
θ_R	Temperature of Q_R	−0.15	°C
θ_i	Ice temperature	−1.0	°C
L	Latent heat of fusion	3.35×10^5	J kg^{-1}
A	Cross-section area of fjord at transect		m^2
V_c	Fjord control volume upstream of A		m^3
Q_M	Submarine meltwater flux		m^3 s^{-1}
Q_R	Runoff (subglacial discharge) flux		m^3 s^{-1}
Q_{FW}	Total freshwater flux		m^3 s^{-1}
Q_{surf}	Volume flux exchanged at air-sea boundary over V_c		m^3 s^{-1}
Q_{glac}	Ice flux (water equiv) at glacier transect		m^3 s^{-1}
Q_{calv}	Calving flux (water equiv)		m^3 s^{-1}
V_{glac}	Ice volume from glacier transect to terminus (water equiv)		m^3
θ	Ocean potential temperature		°C
S	Ocean salinity		g/kg
u	Ocean velocity perpendicular to transect		m s^{-1}
u_0	Mean barotropic velocity $\left(= \overline{\frac{1}{A} \int_A u \, dA} \right)$		m s^{-1}
u_1	Mean baroclinic velocity $(= \overline{u} - u_0)$		m s^{-1}
u_2	Fluctuating velocity $(= u - u_1 - u_0)$		m s^{-1}
$F_{storage}$	Salt storage within V_c		g m^3 kg^{-1} s^{-1}
$H_{storage}$	Heat storage within V_c		W
$H_{melting}$	Latent heat flux to melt ice		W
H_R	Advective heat flux from Q_R		W
H_M	Advective heat flux from Q_M		W
H_{surf}	Air-sea heat flux over V_c		W

mélange forms in winter (Amundson et al., 2020). The water properties within the fjord undergo a strong seasonal cycle: relatively cold and weakly stratified conditions in winter become warmer and more stratified in summer, reflecting seasonality both in source waters from outside the fjord in Frederick Sound and in the freshwater input to the fjord (Amundson et al., 2020; Hager et al., 2022).

2.2. Oceanographic Surveys

We focus here on repeat cross-sections of along-fjord velocity (u), potential temperature (θ), and salinity (S) (Table 1) that were collected over six field campaigns in April and August 2016, May, July, and September 2017, and September 2018 (Table 2). Subsets of these observations were presented in Jackson et al. (2020) (September 2018) and Sutherland et al. (2019) (August 2016 and May 2017); however, each of those studies was limited to one or two seasons, while here we combine six seasons of data to look at freshwater fluxes across a wide range of conditions. In all of the seasons except September 2018, the ship occupied repeat transects at the MB1 sill (Figure 2), recording velocity with both a 600 kHz ADCP (2 m bins from 4 to ∼60 m depth) and 150 kHz ADCP (6 m bins from 10 m to the bottom), and measuring temperature, salinity, and pressure with a profiling CTD. In

Table 2
Average Results for Six Surveying Seasons

Date range	# Transects pairs	Q_{FW} (m^3 s^{-1})	Q_M (m^3 s^{-1})	Q_R (m^3 s^{-1})	Q_{glac} (m^3 s^{-1})	Q_R/Q_M	Q_M/Q_{glac}
01–01 April 2016	2	19 ± 1	8 ± 1	11 ± 1		1.4 ± 0.1	
09–15 August 2016	13	334 ± 102	20 ± 3	314 ± 99	44 ± 2	16 ± 5.6	0.46 ± 0.08
06–10 May 2017	4	37 ± 16	11 ± 2	25 ± 15	35 ± 1	2.2 ± 1.3	0.33 ± 0.05
10–13 July 2017	9	219 ± 49	21 ± 5	199 ± 44		9.6 ± 3	
12–18 September 2017	7	166 ± 99	16 ± 5	150 ± 94	34 ± 1	9.2 ± 6.5	0.49 ± 0.16
13–19 September 2018	10	80 ± 27	12 ± 4	68 ± 23	24 ± 1	5.6 ± 2.7	0.49 ± 0.17

Note. The fluxes of total freshwater (Q_{FW}), submarine meltwater (Q_M), and runoff (Q_R, i.e., subglacial discharge) are calculated from the oceanic budgets. The ice flux into the terminus (Q_{glac}) is calculated from measurements of ice velocity and thickness, and converted into water equivalent so all fluxes are in terms of liquid water. For the ocean-derived quantities, the results are listed as the mean ± standard deviation over the number of transects from that season. The error bounds on the ice flux (Q_{glac}) are derived by varying the ice thickness by ±10 m.

September 2018, the ship occupied transects at various locations between MB1 and the glacier (Figure 2) with a 300 kHz ADCP (4 m bins from 6 to ∼110 m) and a profiling CTD.

Standard processing and quality control for the ADCP data was followed, including the removal of the ship's motion and discarding data near the bottom that was contaminated by sidelobe reflections. The velocity field was then rotated into along- and cross-fjord components, where the along-fjord component is perpendicular to transect lines shown in Figure 2. The along-fjord component of the velocity was then projected onto the transect, averaged over bins that are 30 m wide and 1 m deep, and linearly interpolated in the vertical direction. The temperature and salinity profiles were also projected onto the transect line, bin averaged into the same 30 m × 1 m bins, and then linearly interpolated in the horizontal direction between casts. Velocity required interpolation in the vertical due to the relatively coarse vertical resolution of the ADCPs (∆z = 2 or 6 m) whereas CTD profiles
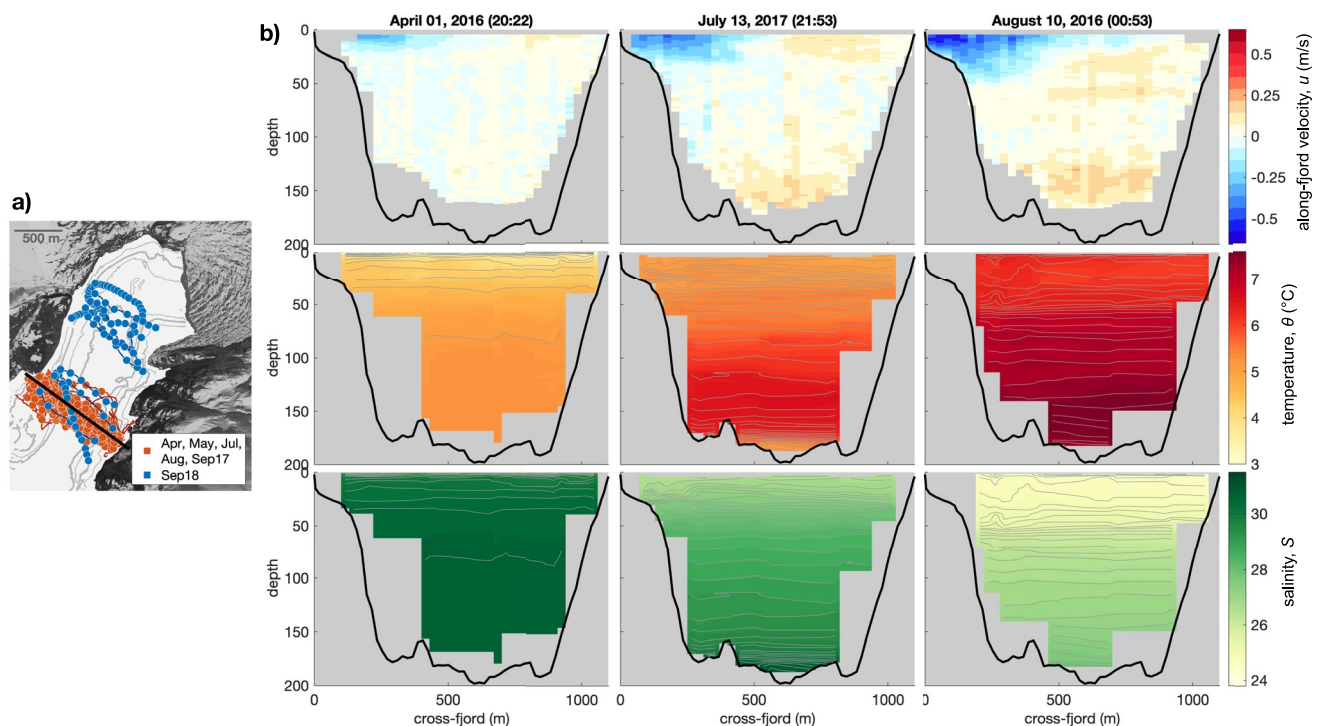
Figure 2. (a) Map of near-glacier region with location of CTDs (dots) and ADCP transects (lines) colored by survey period with September 2018 in blue and all other periods in red. Thick black line shows the transect used for all the surveys except September 2018. Bathymetry contours at 50 m intervals are underlaid. (b) Three sample transects from April 2016, August 2016 and September 2017 of along-fjord velocity (perpendicular to transect in (a)) with positive values toward the glacier, temperature, and salinity. Density contours with intervals of 0.1 kg m^{-3} are overlaid in gray.

required horizontal interpolation due to their relatively coarse resolution in the horizontal ($\Delta x \approx 100$ m between casts, whereas $\Delta z \leq 1$ m).

Finally, we averaged pairs of consecutive transects from the ship transiting out and back across the fjord. We combined pairs of transects for two reasons: to introduce a small temporal average (over ~1.5 hr between occupations) that reduces noise from high frequency fluctuations, and to minimize any residual contamination from the ship's motion in the ADCP velocity. Small errors in removing the ship's motion will largely cancel out when averaging two transects that were occupied in opposite directions. After averaging pairs of transects, we have 45 average sections of u, S, and θ across the six different field campaigns (e.g., three sample sections shown in Figure 2b) that are used to estimate the glacial freshwater fluxes, with methods described in Section 3.

2.3. Glacier Ice Flux

We compare the oceanographic analysis with estimates of glacier ice flux from five glacier field campaigns (four of which overlap with the oceanographic survey periods; Table 2). Ice flux is calculated as $Q_{\text{glac}} \approx \int u_s h \, dx$, where u_s is the glacier surface velocity perpendicular to the transect, h is the ice thickness, and the integral is evaluated over x, the distance along the glacier transect (dashed blue line in Figure 1b). The surface velocity and surface elevation were derived from a terrestrial scanning radar interferometer (Sutherland et al., 2019) for four of the campaigns and from uncrewed aerial vehicle (UAV) surveys for the fifth (Jackson et al., 2020). Surface elevation was combined with bed elevation from multibeam sonar data (Sutherland et al., 2019) to derive ice thickness, with estimated errors on the surface and bed elevation of ± 1 and ± 10 m, respectively. (See Supporting Information S1 for additional details.)

2.4. Surface Mass Balance Model

Subglacial discharge is estimated with an SMB model for LeConte Glacier's catchment basin (as described in Amundson et al., 2020; Jackson et al., 2020; Sutherland et al., 2019). The model couples an Enhanced Temperature Index melt model, an accumulation model, and a linear reservoir-based discharge routing model (Hock, 1999; Hock & Noetzli, 1997). The model was calibrated with four mass-balance stations deployed between 2016 and 2017. A sensitivity analysis was conducted by varying the model parameters within plausible ranges to generate error bars on the output. Between March 2016 and September 2017, the model was forced with data from weather stations deployed on bedrock adjacent to the glacier. To extend the time series into 2018, after the weather stations were decommissioned, we use climate data from Petersburg Airport (40 km from LeConte Glacier), after establishing transfer functions between the two climate records using overlapping data in 2016–2017 (Jackson et al., 2020).

2.5. Other Time Series

In Section 4.5, several previously published time series are incorporated to explore the impact of submarine melting on glacier dynamics over seasonal timescales. We use a time series of the glacier's surface centerline velocity and terminus position derived from time-lapse photogrammetry and a time series of fjord temperature and salinity from a mooring deployed near MB-1 (Amundson et al., 2020; Hager et al., 2022), both covering a 1.5 year period from March 2016 to September 2017.

3. Methods for Estimating Freshwater Fluxes From Oceanic Budgets

We evaluate fjord budgets of heat, salt, and mass to infer the freshwater inputs from the glacier. This general method—alternatively called the fluxgate or fjord budgets method—was pioneered by Motyka et al. (2003, 2013) and first applied to synoptic surveys of LeConte Bay. These methods were further developed in Jackson and Straneo (2016) through a derivation of the complete heat, salt and mass budgets for a fjord and applied to moored records in Sermilik Fjord, Greenland. A growing number of studies have used these methods, either following the approach of Motyka et al. (2003) (e.g., Motyka et al., 2013; Rignot et al., 2010; Xu et al., 2013) or of Jackson and Straneo (2016) (e.g., Cenedese & Gatto, 2016; Schaffer et al., 2020; Sutherland et al., 2019). Other studies use an even simpler framework by estimating melt from the heat flux alone (e.g., Heuzé et al., 2017; Inall et al., 2014;
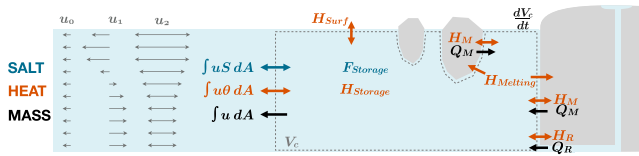
Figure 3. Schematic of fjord budgets of salt (blue), heat (orange), and mass (black), adapted from Jackson and Straneo (2016). The control volume, V_c, is shown with dashed gray line and encompasses all liquid water upstream of the fjord transect, A, where advective fluxes are measured (left side of V_c box). Variables are defined in Table 1.

Johnson et al., 2011), which is only a robust approach if subglacial discharge and other freshwater runoff are small compared to submarine melt (Jackson & Straneo, 2016).

Here we follow the equations and notation of Jackson and Straneo (2016). In Supporting Information S1, we compare these equations with the equations from Motyka et al. (2003, 2013) to reconcile these approaches and illustrate how additional approximations underlie the Motyka et al. (2003, 2013) equations. Since these approximations are not necessary given the data coverage, we follow the more complete equations from Jackson and Straneo (2016).

3.1. Theory

In this method, budgets of heat, salt, and mass are evaluated for a control volume of fjord waters that is bounded by the glacier on one end and a cross-fjord section with oceanic measurements of velocity, salinity, and temperature (u, S, θ) on the other end (Figure 3):

$$\text{Mass:} \int_A u \, dA + \underbrace{Q_R + Q_M}_{Q_{FW}} + Q_{surf} = \frac{dV_c}{dt} \tag{1}$$

$$\text{Salt:} \int_A S u \, dA = \underbrace{\int_{V_c} \frac{\partial S}{\partial t} dV}_{F_{storage}} \tag{2}$$

$$\text{Heat:} \rho c_p \int_A \theta u \, dA + \underbrace{\rho c_p Q_R \theta_R}_{H_R} + \underbrace{\rho c_p Q_M \theta_M}_{H_M} = \underbrace{\rho c_p \int_{V_c} \frac{\partial \theta}{\partial t} dV}_{H_{storage}} + \underbrace{\rho Q_M L_{adj}}_{H_{melting}} + H_{surf} \tag{3}$$

where Q_{FW} is the total freshwater flux into the fjord, which is the sum of liquid freshwater runoff, Q_R, and submarine meltwater, Q_M (Table 1). Runoff could include subglacial discharge and any rivers or surface runoff into the control volume, while submarine melt includes melt from both the glacier terminus and any icebergs melting within the control volume. Q_{surf} and H_{surf} are the surface air-sea fluxes of volume and heat, respectively, θ_M is the temperature of submarine meltwater (seawater freezing temperature), θ_R is the temperature of runoff (assumed to be the freshwater freezing temperature), θ_i is the ice temperature, c_i is the heat capacity of ice, and c_p is the heat capacity of seawater. The adjusted latent heat, $L_{adj} = L + c_i(\theta_M - \theta_i)$, accounts for both the latent heat of fusion, L, and the heat required to raise ice to the melting temperature. Integrals are evaluated either over the cross-sectional area, A, where the fjord transect is made, or over the control volume, V_c, upstream of A. (See Supporting Information S1 for additional details and an explanation of terms.)

Following Jackson and Straneo (2016), the budgets are averaged in time such that the velocity is decomposed in three components: mean barotropic $\left(u_0 = \overline{\frac{1}{A} \int_A u \, dA}\right)$, mean baroclinic $\left(u_1 = \overline{u} - u_0\right)$, and fluctuating $(u_2 = u - u_1 - u_0)$, where overlines denote averaging over a timescale of τ. The salinity and temperature fields are decomposed similarly (into S_0, S_1, S_2 and $\theta_0, \theta_1, \theta_2$, respectively), resulting in three components of the advective salt and heat fluxes through the fjord. Then the total freshwater is inferred as a residual term of the combined salt and mass budgets, and the total freshwater is partitioned into submarine meltwater and runoff using the additional constraint of the heat budget:

$$\overline{Q}_{FW} = \frac{1}{S_0} \left[\int_A u_1 S_1 dA + \underbrace{\overline{\int_A u_2 S_2 dA} - \overline{\int_{V_c} \frac{\partial S}{\partial t} dV}}_{\text{neglect}} \right] \tag{4}$$

$$\overline{Q}_M = \frac{c_p}{L_{adj} - c_p(\theta_M - \theta_R)}\left[\overline{Q}_{FW}(\theta_R - \theta_0) + \int_A u_1\theta_1\, dA + \underbrace{\overline{\int_A u_2\theta_2\, dA} - \overline{\int_{V_c} \frac{\partial\theta}{\partial t}\, dV} - \frac{H_{surf}}{\rho c_p}}_{\text{neglect}}\right] \tag{5}$$

$$\overline{Q}_R = \overline{Q}_{FW} - \overline{Q}_M \tag{6}$$

In this application for LeConte Bay, we neglect the storage terms, the surface fluxes, and the fluctuating transports (indicated by underbraces in Equations 4–6), with justification for neglecting these terms in the following section. We emphasize that the assumptions behind dropping these terms will not be valid at many other glacier-fjord systems.

3.2. Application of Method to Data and Error Analysis

In order to calculate the freshwater fluxes from the simplified version of Equations 4–6, we use the sections of velocity, temperature, and salinity to evaluate u_1, S_1, S_0, θ_1, and θ_0. The observations, however, have incomplete spatial coverage over the fjord cross-section, with gaps at the surface, sides, and bottom (Figure 2). For the velocity field, we use two methods to extrapolate to the surface, two methods to extrapolate to the bottom and sides, three options for a tidal adjustment, and three options for enforcing mass conservation, resulting in 36 permutations of the complete u_1 field (see Supporting Information S1). The temperature and salinity fields are extrapolated horizontally to the sides of the fjord assuming a constant value equal to the nearest CTD cast, based on the weak cross-fjord gradients observed in water properties. The extrapolated θ and S sections are decomposed into θ_1, θ_0, S_1, and S_0.

For each of the 45 transects, we calculate the freshwater fluxes using all 36 permutations of the u_1 field. We report the final results ($\overline{Q}_{FW}$, $\overline{Q}_R$ and $\overline{Q}_M$, and hereafter we drop the overlines) for each transect as the mean of the 36 values, and the standard deviation is one component of the error bounds (with the other component arising from the unresolved temporal variability, as discussed in Section 3.2.1). As such, we use the spread in these extrapolation methods to quantifying the uncertainty that arises from incomplete spatial coverage of the data.

The runoff and submarine melt fluxes are primarily presented as volume fluxes ($m^3\,s^{-1}$) of freshwater, but we also convert the melt flux into a spatial-average of the terminus melt rate ($m\,d^{-1}$) using the average submarine terminus surface area of $146 \times 10^3\,m^2$ (Sutherland et al., 2019) and taking into account the density difference between liquid water and ice. This conversion assumes that Q_M is entirely derived from terminus melt, neglecting any input of submarine melt from icebergs. Thus, the volume flux of Q_M is a more robust estimate of the total meltwater flux, while the average terminus melt rate should be considered an upper limit due to the unresolved contribution of icebergs. Additionally, by using a constant terminus surface area, the melt rate neglects the seasonal changes in submarine surface area (Eidam et al., 2020). The runoff flux, Q_R, could include any inputs of freshwater that do not require latent heat from the ocean to undergo phase change, but we assume that runoff is dominated by subglacial discharge that drains at the bed of the glacier. In summary, we interpret Q_M as the submarine melt of the glacier and Q_R as subglacial discharge, and we further explore the validity of these assumptions below.

Since the sections considered here are derived from averaging two consecutive fjord transects, approximately 1.5 hr from start to finish, we consider our averaging timescale, τ, to be only ~1 hr. While this is a very short timescale (e.g., compared to the 30-day averaging timescale used for Sermilik Fjord in Jackson & Straneo, 2016; or a typical 1-day timescale used to average over the tidal cycle in standard estuaries, e.g., Lerczak et al., 2006), the high-frequency variability in these near-glacier sections is relatively small compared to the mean signal.

3.2.1. Error Estimates

There are two components of uncertainty that go into our error bars: an estimate of the error from incomplete spatial coverage of the transect data, $Q^{err,\,spatial}$ and an estimate of the unresolved temporal variability, $Q^{err,\,temp}$. As outlined in the previous section, $Q^{err,\,spatial}$ is derived from the 36 permutations of the extrapolation methods, and this is the dominant source of error in our freshwater estimates.

We also estimate the error from neglecting any temporal variability that would result in heat/salt storage terms (F_{storage} and H_{storage} in Equations 4–6). Our observations do not allow us to explicitly resolve these storage terms for each transect calculation, but we estimate a maximum value for each season as follows. We calculate the change in section-averaged salinity and temperature, S_0 and T_0, between transects and determine the maximum observed value for $\frac{\partial S_0}{\partial t}$ and $\frac{\partial T_0}{\partial t}$ in each season. Then, we make an approximation that the variability in S_0, the area-averaged salinity at the cross-section, is similar in magnitude to the variability of the volume-averaged salinity within the control volume, so that we can approximate the last term in Equation 4 as $\frac{1}{S_0} \int_{V_c} \frac{\partial S}{\partial t} dV \approx \frac{1}{S_0} \frac{\partial S_0}{\partial t} V_c$. This allows us to estimate the error in Q_{FW} from neglecting the salt storage term, $Q_{FW}^{err,temp}$, which we find ranges in value from 1.3 m³ s⁻¹ in May to 9.5 m³ s⁻¹ in August. This contributes a very small error that is <3% of the magnitude of Q_{FW} in all seasons, whereas $Q_{FW}^{err,spatial}$ is, on average, 18% of the freshwater magnitude. Similarly, we estimate an upper bound on the heat storage term from the variability in T_0, and we find that neglecting the heat storage term results in an error that ranges from 1.1 m³ s⁻¹ in August to 3.2 m³ s⁻¹ in July. This contributes a 5%–25% error relative to the magnitude of Q_M. Using our estimates of the upper limit of heat/salt storage terms, we propagate these terms through Equations 4–6 to calculate the total error from neglecting temporal variability, for example, $Q_M^{err,temp}$.

Finally, for each averaged transect, we add the spatial and temporal errors together in quadrature, under the assumption that they are uncorrelated, to generate the complete error bars: for example, $Q_M^{err} = \sqrt{\left(Q_M^{err,spatial}\right)^2 + \left(Q_M^{err,temp}\right)^2}$, and similarly for Q_R and Q_{FW}. The final results are reported as $Q_M \pm Q_M^{err}$ for each averaged transect.

3.2.2. Other Neglected Terms and Assumptions

Aside from the storage terms, the other terms that have been neglected in calculating the freshwater fluxes from Equations 4–6 are surface heat fluxes and fluctuating heat and salt transports. We briefly justify each of these assumptions:

1. **Neglecting surface heat flux**. The surface heat flux (H_{surf}) is compared to the latent heat flux to melt ice (H_{melting}) in order to demonstrate that H_{surf} can be neglected in this application. The latent heat required to produce 8 m³ s⁻¹ of meltwater—the average in April 2016, when the melt flux was lowest—is 3.0×10^9 W. A relatively high surface heat flux of 200 W m⁻² (e.g., Jackson & Straneo, 2016) over the 1 km² surface area of the control volume would produce $H_{\text{surf}} = 2 \times 10^8$ W. Thus, even a high value for H_{surf} would be an order of magnitude smaller than the low values of latent heat, and we argue that neglecting the surface heat flux will introduce an error that is substantially smaller than the error bars.

2. **Neglecting fluctuating transports**. Correlations between u_2 and θ_2 or S_2 can result in a fluctuating (i.e., eddy) transport of heat and salt. In this application, the averaging timescale is very short—we only average between consecutive pairs of transects—so u_1 is an estimate of the velocity averaged over ~1.5 hr, and we do not resolve u_2, which would be the component of u at higher frequencies. Additionally, if there were a significant eddy flux at periods longer than 1.5 hr (e.g., associated with the tides) then it would show up in the u_1 component of the advective transports and one would expect the baroclinic salt/heat flux—and estimated freshwater fluxes—to fluctuate with the tidal phase. However, we find no significant correlation between these calculated quantities and the tidal phase, suggesting that any tidal heat and salt fluxes are relatively small at the location of our transects. An examination of the transects and mooring records in Amundson et al. (2020) suggest that the buoyancy-driven exchange flow is the largest component of the velocity field during our survey periods, which reduces the likelihood of a significant eddy flux (e.g., Jackson & Straneo, 2016).

   Finally, we make an additional set of assumptions when we interpret Q_M as glacier submarine melt and Q_R as subglacial discharge:

3. **Neglecting freshwater from iceberg melt and surface runoff**. We estimate that iceberg melt should be a relatively small contribution given the close proximity of the transects to the glacier (i.e., small control volume) and the fact that the surface waters were not ice-choked during the surveying periods. To provide a back-of-the-envelope estimate, we combine the following facts: (a) the control volume represents approximately 7% of the fjord surface area; (b) most of the icebergs melt within the fjord, (c) most icebergs quickly transit through the control volume (Kienholz et al., 2019). If we combine these observations to assume that the entire calving flux becomes iceberg submarine melt that is uniform distributed throughout the fjord and further assume that the submarine melt flux is approximately equal to the calving flux (as the results of this paper suggest), then the iceberg melt within the control volume would be ~7% of the submarine meltwater
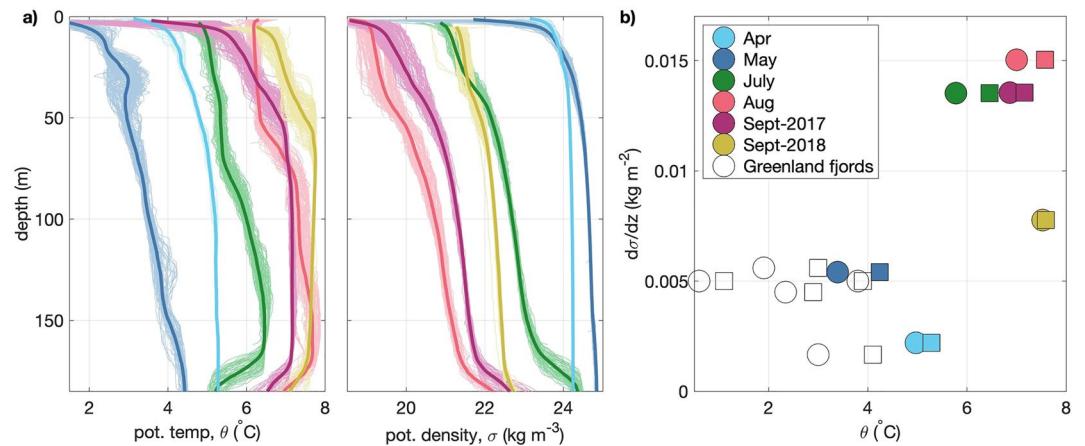
Figure 4. (a) Temperature and density profiles from all CTD casts across the transect (thin lines) and their average (thick lines) in each of the survey periods. (b) Parameter space of average density stratification (10 m to grounding line depth) versus temperature. Squares show grounding line temperature while circles indicate depth-averaged temperature. Black symbols are from four major fjords in Greenland: Kangerlussuup and Rink fjords in central west Greenland, and Kangerlugssuaq and Sermilik fjords in southeast Greenland.

flux. By this estimate, iceberg melt would introduce an error that is smaller than the error bars calculated from spatial and temporal variability that are explicitly included in our results. However, we note that this is only a crude approximation and thus icebergs are a source of un-quantified uncertainty in our results for Q_M. Additionally, we assume that Q_R represents the subglacial discharge, based on the absence of any significant surface runoff into the control volume and an assumption that subaerial melt of icebergs is negligible, and thus we use the term "subglacial discharge" to refer to Q_R in the following sections.

4. Results

The surveys span a wide range of conditions in fjord temperature, salinity, and stratification (Figure 4). The fjord is generally warmer and more strongly stratified in July, August, and September, while cooler and more weakly stratified conditions occur in April and May. The variability in fjord conditions within each surveying period is relatively small compared to the variability between seasons (Figure 4a). Also shown for comparison in Figure 4b are the conditions from four major fjords in Greenland: summertime conditions (July or August) from Kangerlussuup and Rink fjords in central west Greenland, and Kangerlugssuaq and Sermilik fjords in southeast Greenland; and also wintertime conditions (March) from Sermilik fjord (Bartholomaus et al., 2016; Straneo et al., 2012). The Greenlandic conditions are similar to the spring conditions in LeConte Bay. Thus, the parameter space explored in this data set overlaps with Greenlandic fjords while also extending to conditions that are much warmer and more stratified than Greenland.

In all of the fjord cross-sections, we observe an outflowing plume—at or near the surface—and a return flow toward the glacier at depth (Figure 2). This circulation varies in strength, with the strongest flow in summer (July and August) and the weakest flow in spring (April and May). This exchange flow, presumably driven by glacial freshwater, is the dominant signal in the sections, though we also expect a smaller signal from tides and other modes of circulation.

The average freshwater fluxes for each surveying period are reported in Table 2 (also plotted later in Figure 8), while the individual values for each transect pair are shown in Figure 5. The mean meltwater flux varies from 8 m³ s⁻¹ in April to 21 m³ s⁻¹ in July, while subglacial discharge spans a wider range from 11 to 314 m³ s⁻¹. In the spring surveys, submarine melt and subglacial discharge are similar orders of magnitude ($Q_R/Q_M = 1.4 \pm 0.1$ and 2.2 ± 1.3 in April and May, respectively), while in the summer the subglacial discharge is an order of magnitude larger ($Q_R/Q_M = 16 \pm 5.6$ in August).
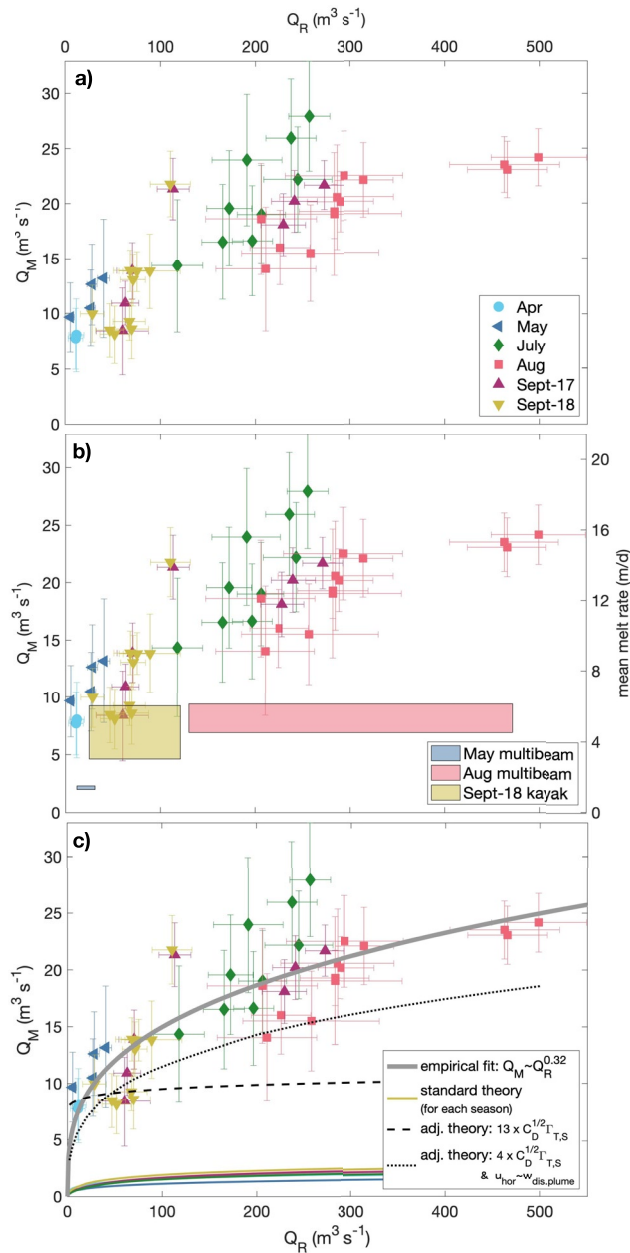
Figure 5. In all panels: submarine melt versus subglacial discharge from budgets, colored by surveying period. (a) Includes the legend for the surveying periods. (b) Includes melt rates from multibeam sonar (Sutherland et al., 2019) and kayak profiling (Jackson et al., 2020). Right-side vertical axis is the mean melt rate in m d⁻¹ of ice, from dividing the meltwater flux by the submarine terminus area and converting from liquid water to ice. (c) Includes empirical best fit to observations, $Q_M \sim Q_R^{0.32}$, standard plume-melt theory for each season, with colors corresponding to the seasonal colors in the legend of (a), and adjustments to theory proposed by Jackson et al. (2020) based on kayak surveys.

4.1. Subglacial Discharge: Comparison With SMB Model

We compare the ocean budgets estimate of subglacial discharge with the SMB model's estimate for subglacial discharge in Figure 6a. These ocean surveys capture a range of discharge conditions, as predicted by the SMB model and also reflected in the budgets estimates: low subglacial discharge in April and May surveys, moderate discharge in both Septembers and July, and highest discharge in August.

The maximum lagged correlation between the SMB model and the ocean budgets occurs at −1.0 day lag, with the SMB model leading the ocean budgets. At this lag, a linear regression has a best-fit slope of 0.9 with $R^2 = 0.76$, suggesting a relatively strong agreement in the subglacial discharge estimates from the SMB model and from ocean budgets (Figure 6b). It is not immediately obvious which estimate of subglacial discharge should be considered more accurate. Neither method of estimating discharge has been validated at a marine-terminating glacier. However, their agreement in this comparison is promising for both approaches, and provides a novel data set for comparing these two methods for estimating subglacial discharge fluxes: at the upstream end from a data-informed SMB model, and at the downstream end from fjord budgets. Notably, these two estimates are entirely independent, with no overlap in the data that is used for each calculation.

The maximum correlation at −1.0 day lag is not significantly higher than the correlation at 0 lag ($R^2 = 0.76 \pm 0.13$ and $R^2 = 0.64 \pm 0.17$, respectively, with 95% confidence intervals), although the correlation drops significantly at lags larger than −1.4 days. Two processes could contribute to such a lag with bounds between −1.4 and 0 days: (a) the oceanic advection from the terminus to MB-1 sill (which we estimate to be only ∼1 hr based on fjord velocities), and (b) an underestimation of the storage/transit time in the linear reservoir model within SMB model (Amundson et al., 2020; Sutherland et al., 2019).

4.2. Submarine Melt: Comparison With Multibeam and Kayaks

The submarine meltwater fluxes are converted to an average terminus melt rate of 5–18 m d⁻¹ and compared to two independent estimates (Figure 5b): melt rates derived from repeat multibeam sonar scans in May 2017 and August 2016 (Sutherland et al., 2019) and from kayak surveying near the terminus in September 2018 (Jackson et al., 2020). The kayak-derived melt estimate overlaps with the budgets estimate for September 2018, within their error bars. The multibeam-derived melt estimates fall below the range of the budget estimates, though they are the same order of magnitude.

Regarding the discrepancy between multibeam and ocean budgets, we note that, while multibeam provides a robust estimate of melting over localized swaths of the terminus, its incomplete spatial coverage means that the average multibeam melt rate should be biased low if considered as a terminus-wide average. Melt rates are only calculated in areas without calving events, thus any spatial correlation between calving and melting would bias the multibeam rates low. Additionally, the multibeam melt rates are sparse in the region of the main subglacial discharge plume, where melt appears to be significantly higher than other portions of the terminus. If the missing area of plume-enhanced melt were 10%–20% of the terminus, then plume-driven melt rates of 25–45 m d⁻¹ over this area would be necessary to close the gap between the budgets and multibeam melt in August. The lower end of this range is plausible (given the distribution of multibeam melt rates) while the upper end is not (given the ice velocity), suggesting that the limited spatial coverage of the multibeam could
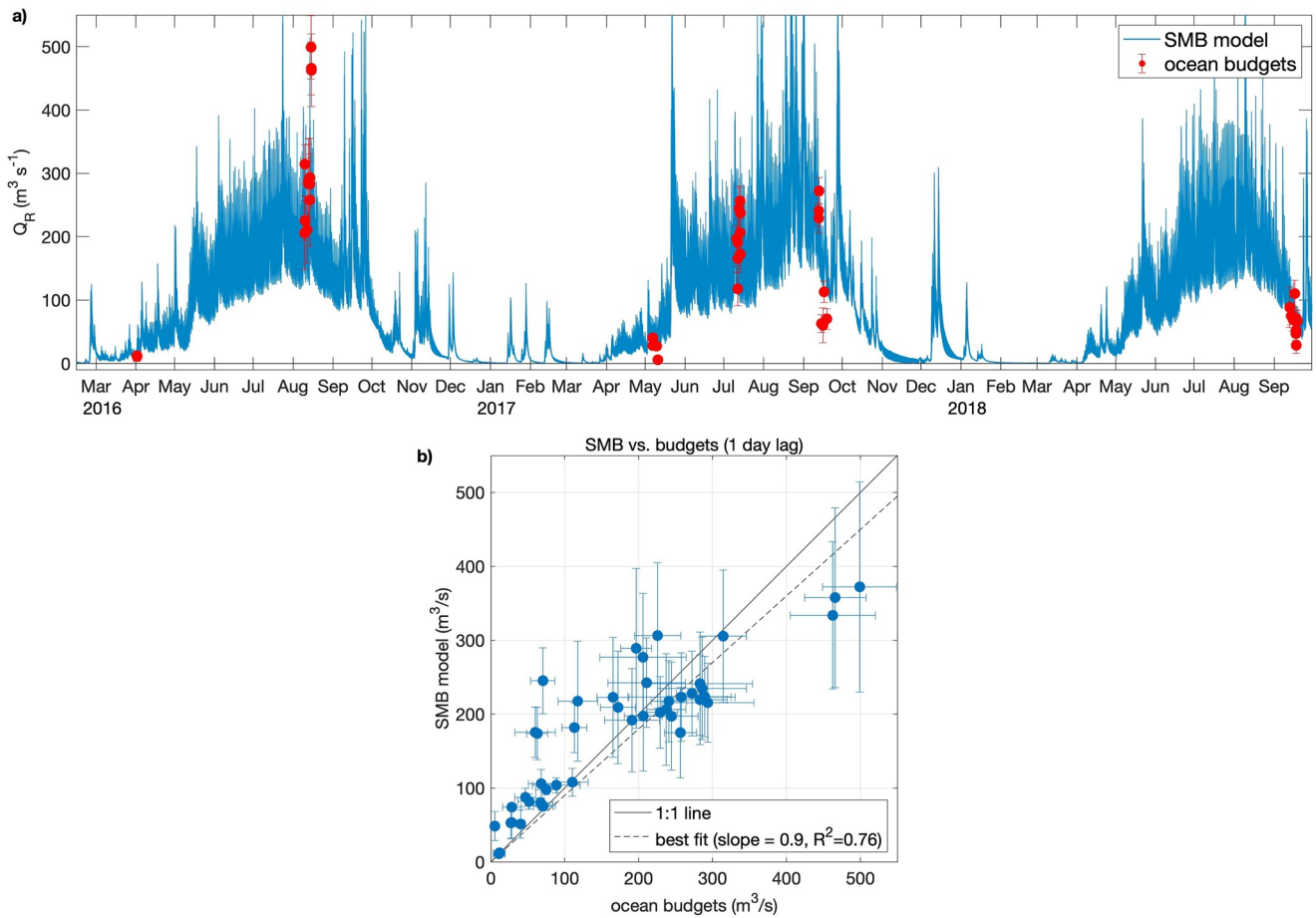
Figure 6. Comparison of subglacial discharge between SMB model and ocean budgets: (a) time series; (b) SMB model versus ocean budgets at 1 day lag (maximum lagged correlation). Solid line is 1:1 and dashed line is the best fit slope (forced through zero).

explain a significant but unknown portion of the discrepancy. Additionally, the budgets estimate of terminus melt would be biased high if iceberg meltwater contributes to the total meltwater flux within the fjord control volume (see Section 3.2.2).

Overall, the three different estimates of submarine melting—surveying of meltwater intrusions by kayaks, downstream fjord budgets, and multibeam terminus surveying—provide melt rates that are a similar order of magnitude. Each of these three estimates is entirely independent, with no overlap in the data products used. Furthermore, all three estimates of melt are at least an order of magnitude larger than standard estimates derived from theory, as will be shown in Section 4.4.

4.3. Submarine Melt as a Fraction of Ice Discharge

We compare the total submarine melt flux with estimates of the total ice flux near the terminus for the four surveys where we have both measurements (Table 2). Across these survey periods, there is substantial variability in the average melt rate (11–20 $m^3 \ s^{-1}$) and the ice flux (24–44 $m^3 \ s^{-1}$ water equivalent), yet the ratio of melt to ice flux, Q_M/Q_{glac}, falls within a somewhat narrow range of 0.33–0.49. This indicates that submarine melting accounts for approximately one third to one half of the ice flux into the terminus across a range of conditions in spring, summer, and early fall. While difficult to generalize from only four data points, the summer and early fall values of Q_M/Q_{glac} lie at the upper end of this range (0.46–0.49), while a lower ratio is found in spring (0.33).

4.4. Submarine Melt as a Function of Subglacial Discharge and Fjord Conditions

The relationship between submarine melt and subglacial discharge is explored in Figure 5, showing a positive correlation between these two quantities as expected from previous observations at LeConte (Motyka et al., 2013) and from modeling and theoretical studies (e.g., Jenkins, 2011; Sciascia et al., 2013; Slater et al., 2016).

In Figure 5c, predictions from plume-melt theory are compared with the observations. We calculate "standard" theoretical predictions based on the following assumptions: (a) standard empirical values for transfer and drag coefficients, derived from ice shelf studies (e.g., Cowton et al., 2015; Jenkins, 2011); (b) the upwelling convective velocities from meltwater and subglacial discharge are the only velocities driving transfer across the boundary layer; and (c) the discharge plume rises as a 200-m wide truncated line plume. While a 100-m wide plume is the best guess based on LeConte observations (e.g., Jackson et al., 2017), we use twice this width to assess an approximate upper limit on total melt based on either a wider plume or the presence of two plumes (suggested by surveying in September 2018, but unlikely in other survey periods). As explored in Jackson et al. (2020) and discussed further below, there are potential pitfalls to these assumptions, but this setup of plume-melt theory is shown as the benchmark for "standard" theory as commonly implemented in previous literature. The theoretical curves for total melt in Figure 5c include both discharge-driven melt and ambient melt, though ambient melt is almost negligible in this formulation so the total melt almost exactly follows the discharge-driven regime scaling of $Q_M \sim Q_R^{1/3}$. There is a different theoretical curve for each season, based on the average fjord temperature and salinity profile from each field campaign (see Figure 4).

The best exponential fit between the budget estimates of melt and discharge is $Q_M = 3.5Q_R^{0.32}$, with 95% confidence bounds on the exponent of $\alpha = 0.32 \pm 0.07$ (Figure 5c). This compares favorably to the 1/3 exponent predicted by standard theory (Jenkins, 2011; Slater et al., 2016). While the observations and theory both show a similar exponential scaling between melt and discharge, the observed melt flux is an order of magnitude larger than the estimates from theory with standard coefficients (Figure 5c). Broadly this aligns with previous results from Jackson et al. (2020) and Sutherland et al. (2019)—both papers showed that the standard application of theory underpredicts melt rates—but here this discrepancy can be explored across a wide parameter space of forcing conditions to examine the relationship between subglacial discharge and submarine melt. In the Discussion Section, we discuss possible modifications to "standard" theory that might explain why the exponential relationship between melt and discharge holds while the overall magnitude of melt is under-predicted.

We also explore the dependence of melt on fjord temperature and stratification, with the surveys spanning a range of fjord conditions. Based on standard theory, we might expect melt to scale linearly with thermal forcing, $\theta - \theta_f$, where θ_f is the freezing temperature of seawater (e.g., Jenkins, 2011; Slater et al., 2016). A simple attempt at including this linear dependence on thermal forcing does not improve the fit between melt and discharge: a linear regression between Q_M and $Q_R^{0.32}$ has an R^2 of 0.71, while R^2 drops to 0.54 for a regression between Q_M and $Q_R^{0.32}(\theta_{ave} - \theta_f)$. We perform these analyses with both the depth-averaged temperature, θ_{ave}, and the grounding line temperature, θ_{GL}, but find no significant difference in their correlation (or lack thereof) with submarine melt, so here we show only the analysis with θ_{ave}.

In Figure 7, we further explore the dependence of melt on the three potential controls that we observe: subglacial discharge, fjord temperature, and fjord stratification. When comparing melt versus discharge and melt versus thermal forcing (Figure 7a), the dependence of melt on discharge is more apparent than the dependence of melt on fjord conditions. Next, we attempt to remove the discharge dependence $\left(Q_M/Q_R^{0.32}\right)$ and examine if the residual variability in melt is correlated with fjord conditions (Figure 7b). We find that there is no significant correlation between $Q_M/Q_R^{0.32}$ and the thermal forcing, and the weak negative slope of the linear regression is unrealistic if melt approaches zero as thermal forcing goes to zero. Similarly, a regression analysis with fjord stratification $\left(\frac{\partial \rho}{\partial z}\right)$ and with the combination of fjord stratification and thermal forcing $\left((\theta - \theta_f)/\sqrt{\frac{\partial \rho}{\partial z}}\right)$, suggested by theory (e.g., Magorrian & Wells, 2016) does not reveal a significant correlation. In both cases the best-fit slope is indistinguishable from zero within the uncertainty bounds (dashed lines in Figure 7).

Thus, we cannot discern any clear dependence of melt on fjord conditions, even after removing the discharge dependence. We suspect there is, in reality, a relationship between melt and fjord conditions, but there are several reasons that it might be difficult to isolate this relationship. First, the subglacial discharge forcing spans a much wider range of conditions ($Q_R = 5$–500 m^3 s^{-1}) than the thermal forcing ($\theta_{ave} - \theta_f = 5.0$–9.2°C). If melt scales as
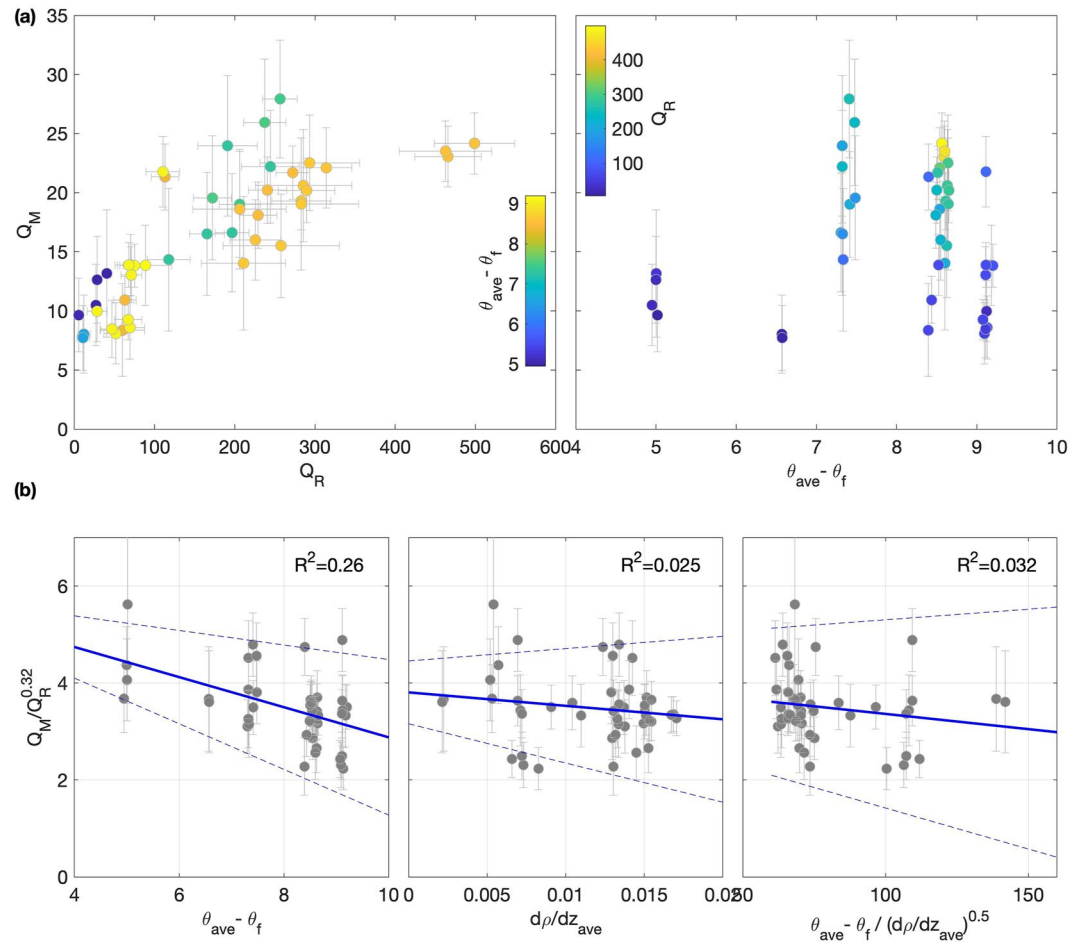
Figure 7. (a) Melt versus subglacial discharge with thermal forcing in color, left, and melt versus thermal forcing, with subglacial discharge in color, right. (b) $Q_M/Q_R^{0.32}$, which is melt with the discharge-dependence removed, versus thermal forcing, density stratification, and combination of the two as suggested by theory. Linear regressions are shown in blue, with 95% confidence intervals in dashed lines and R^2 values in the upper right.

$Q_M \sim Q_R^{1/3}(\theta - \theta_f)$ as theory predicts, then the difference between the maximum and minimum thermal forcing (5 vs. 9.2°C) would result in an 84% increase in melt. On the other hand, the difference between the maximum and minimum subglacial discharge (5 vs. 500 m^3 s^{-1}) would result in a 360% increase in melt. Thus, the variability in melt associated with discharge would be much larger and easier to observe in a noisy data set compared to the variability associated with fjord conditions.

Additionally, the temperature variability within each survey period is small (Figures 4 and 7a) so there are effectively only six independent measurements to examine melt versus temperature, whereas subglacial discharge varies significantly within each survey period so that each transect pair can be regarded as an approximately independent measurement of melt versus discharge (45 total). For these reasons, our analysis provides more insight into the dependence of melt on discharge than on fjord conditions.

4.5. Seasonality of Ocean Forcing and Glacier Behavior

To put the submarine meltwater fluxes in the context of glacier variability, we assess the mass budget of ice between the glacier transect (Figure 1) and the terminus:

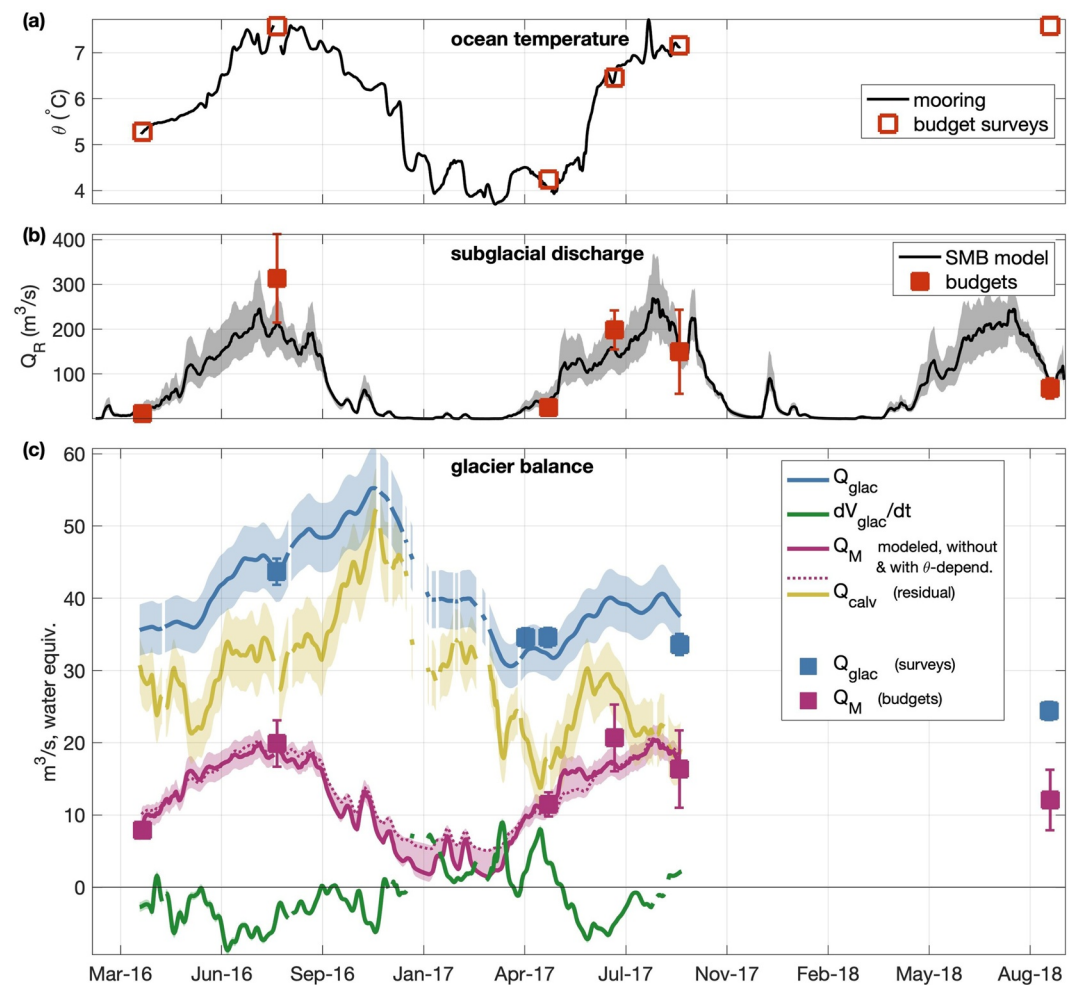$$\frac{dV_{glac}}{dt} = Q_{glac} - Q_M - Q_{calv} \tag{7}$$

Figure 8. Time series from March 2016 to September 2018. (a) Temperature from upper-fjord mooring at 150 m depth in black, with the average grounding-line temperature from each shipboard survey in red. (b) Subglacial discharge from the SMB model and from ocean budgets averaged over each survey period, with error bars indicating the standard deviation between transects. (c) Ice flux, Q_{glac}, measured directly (blue squares) and estimated indirectly from the time series of centerline ice velocity (blue line); submarine melt flux, Q_M, from the budgets averaged over each season (purple squares) and modeled melt from the two empirically derived scalings, with and without a temperature dependence (dashed and solid purple lines, respectively); change in ice volume, $\frac{dV_{glac}}{dt}$ (green line); and calving flux, Q_{calv}, calculated as a residual of Q_{glac}, $\frac{dV_{glac}}{dt}$ and Q_M (yellow line).

where V_{glac} is the ice volume between the glacier transect and the terminus, Q_{glac} is the ice flux through the glacier transect, Q_M is still the submarine melt flux, and Q_{calv} is the iceberg calving flux. We neglect subaerial surface melt given the small surface area between the glacier transect and terminus.

4.5.1. Constructing Time Series of Glacier Mass Budget

We calculate a timeseries of $\frac{dV_{glac}}{dt}$ (green line in Figure 8c) by assessing advance/retreat from the time-lapse record of terminus position and thickening/thinning from the DEM data. To construct a time series of Q_{glac} (blue line in Figure 8c), we compare the radar and UAV ice flux surveys with the 1.5-year time series of centerline ice velocity derived from time-lapse photogrammetry (Amundson et al., 2020; Sutherland et al., 2019) to derive an empirical relationship between centerline velocity and total ice flux. We then use this velocity-flux relationship to construct a time series of ice flux, Q_{glac}, from the centerline velocity time series. Details of these calculations and their associated uncertainties are presented in Supporting Information S1.

We create a time series of modeled melt, Q_M, with the exponential regression between Q_M and Q_R from the oceanic budgets ($Q_M = 3.5Q_R^{0.32}$, Figure 5). Using this equation with the time series of Q_R from the SMB model

(Figure 8b), we derive a modeled melt time series (solid purple in Figure 8c). We also include the empirical best-fit between Q_M and $Q_R^{0.32}(\theta - \theta_f)$ (dashed purple line) where the time series of θ is derived from the upper-fjord mooring (Figure 8a, Amundson et al., 2020). Although we have shown that the inclusion of thermal forcing provides a worse fit to the data (Section 4.4), we include this scenario to show how a linear dependence on $\theta - \theta_f$ has a relatively small impact on melt compared to the variability in subglacial discharge. The purple-shaded error bars represent the range from using the upper and lower bounds on the SMB model and both forms of the empirical melt model with and without temperature dependence.

With these independently calculated time series of Q_{glac}, $\frac{dV_{glac}}{dt}$, and Q_M, we then infer Q_{calv} (yellow line in Figure 8c) as the residual using Equation 7.

4.5.2. Seasonality and Correlation Between Glacier Budget Terms

The time series of modeled submarine melt follows a similar seasonal pattern as subglacial discharge, peaking in summer and dropping by almost an order of magnitude in winter as subglacial discharge shuts down and as ocean temperature decreases by 3.5°C (Figure 8). Changes in glacier volume, which largely reflect the terminus position's variability, show retreat of ∼500 m in both summers and advance in winter. The ice flux peaks in fall 2016, reaches a minimum in early spring 2017, and then rebounds into the following summer. Calving follows a similar seasonality as the ice flux, with a similar magnitude to melting in summer and almost an order of magnitude larger than melting in winter.

A relatively robust anticorrelation ($R = -0.68$, $p < 0.05$) exists between Q_M and $\frac{dV_{glac}}{dt}$, indicating that the seasonal retreat of the glacier coincides with periods of enhanced submarine melting. The correlation between Q_M and Q_{glac} is not statistically significant, suggesting that submarine melt has little direct influence on ice flux to the terminus but, as we explore in Section 5.4, it may have an indirect impact by forcing the terminus into deeper water and thereby increasing calving. Additionally, the ice flux and glacier volume change have a negative correlation ($R = -0.3$, $p < 0.05$), indicating glacier advance during periods of lower ice flux and retreat during higher ice flux.

There is a weak negative correlation between melt and calving, but we do not report this as a result because calving is calculated as function of $-Q_M$ (Equation 7), so any errors or noise in the melt time series will contribute to a spurious anti-correlation between melt and calving. The correlation coefficients listed above are only reported for the time series that are estimated independently.

5. Discussion

5.1. Fjord Budgets at LeConte and Elsewhere

The oceanic observations presented here provide a novel data set for measuring submarine melt and subglacial discharge across a wide range of oceanic and atmospheric conditions. This is possible, in part, because we are able to reduce the full fjord budget equations (Equations 4–6) to a simplified version that is tractable with synoptic surveys. This simplification relies on three approximations—neglecting surface fluxes, fluctuating transports, and storage terms (though the last term is included in our error bars)—which we argue are valid approximations due to the particular conditions at LeConte: a strong signal of the freshwater-driven circulation, weak variability from other modes of circulation, and relatively open waters, which allow for a small control volume. We emphasize that these approximations could introduce significant errors in other applications, for example, in fjords with large temporal variability or with measurements made far from a glacier.

Additionally, in Supporting Information S1, we reconcile the equations presented here (based on the framework of Jackson & Straneo, 2016) with the equations from Motyka et al. (2013), and demonstrate how three further assumptions, in addition to the three listed above, underlie the latter approach. We note that the results presented in Motyka et al. (2013) for late summer 2012 overlap with the summer results presented in this paper (Figure S2 in Supporting Information S1). This is likely because the three additional assumptions of Motyka et al. (2013) are reasonably valid approximations for LeConte Glacier. (These assumptions are not necessary in this paper, given the data coverage.) On the other hand, these additional assumptions could become problematic in fjords with a more complex velocity structure. Thus, as a general method, we advocate for future studies to start with

the full budget equations (Jackson & Straneo, 2016) and to only drop terms based on the particular fjord system in question.

5.2. Seasonality of Freshwater Fluxes

The oceanic budgets reflect a wide range of total freshwater fluxes, from an average of 19 m³ s⁻¹ in April to 334 m³ s⁻¹ in August (Table 2, Figure 8). In the spring surveys, submarine melt and subglacial discharge are similar in magnitude, whereas subglacial discharge is an order of magnitude larger than submarine melt in summer and early fall. Thus, the high freshwater input in summer, corresponding to high buoyancy-forcing of the fjord, is dominated by subglacial discharge, while in spring, submarine melt contributes a larger portion of the much weaker freshwater forcing.

We can further examine the seasonality of freshwater forcing with the SMB model, which has been shown to compare well with the oceanic budgets, and the time series of modeled melt (Figures 8b, 8c). These time-series indicate that submarine melt has a similar seasonality as subglacial discharge; however, the ratio of discharge to modeled melt varies significantly throughout the year, with discharge being dominant in summer (as confirmed by the ocean budgets) and submarine meltwater being a factor of 2 larger in winter. However, the comparison between modeled melt and discharge should be treated with caution in winter, given the lack oceanic measurements during this period. The empirical model for melt as a function of discharge was derived from spring, summer, and early fall conditions when $Q_R \geq 10$ m³ s⁻¹. Based on previous theoretical studies, there is reason to suspect that the relationship between Q_M and Q_R might follow a different scaling law in the limit of $Q_R \to 0$ (Jenkins, 2011; Slater et al., 2016).

Overall, these seasonal patterns in submarine melt and subglacial discharge are broadly aligned with theoretical and modeling predictions (e.g., Cowton et al., 2015; Sciascia et al., 2013) and previous work at LeConte that shows higher melt rates in August compared to May (Sutherland et al., 2019). Additionally, Moffat et al. (2018) examine the seasonality in freshwater fractions within a Patagonian glacial fjord, finding ratios of Q_R/Q_M near 0.9 in wintertime (similar to our results) and 2.5 in summertime (lower than our results), though these ratios are based on freshwater fractions in the fjord, not flux estimates. Previous observational studies that quantify the fluxes of subglacial discharge and submarine melt fluxes have typically been limited to short periods of days or weeks (e.g., Inall et al., 2014; Jackson et al., 2020; Motyka et al., 2013) or limited by large error bars (Jackson & Straneo, 2016), such that the interdependence of melt and discharge and their seasonality is not discernible.

5.3. Theory for Submarine Melting

5.3.1. Exploring Adjustments to the Common Parameterization

Here, we explore the discrepancy between our observations and predictions from theory (Figure 5c). Our results suggest that melt scales exponentially with discharge in a way that is consistent with "standard" plume-melt theory $\left(Q_M \sim Q_R^{1/3} \right)$, but the overall magnitude is substantially higher than theoretical estimates using standard empirical coefficients.

The results presented here add further evidence that ambient melt is a non-negligible portion of the total melt, in line with observations from Sutherland et al. (2019) and Jackson et al. (2020) and contrary to the standard application of plume-melt theory. If the summer melt fluxes of 25 m³ s⁻¹ were concentrated behind a discharge plume of 200 m width, then the local discharge-driven melt rates would be ~55 m d⁻¹. Combined with the ice velocity of 28 m d⁻¹, this would imply a persistent retreat of ~27 m d⁻¹ at the discharge plume location, which is not realistic (the maximum observed retreat was 4 m d⁻¹). Thus the total submarine melt flux is too high to be driven primarily by a classic, localized discharge plume and instead must be distributed more broadly across the terminus.

Several adjustments to standard theory were suggested by Jackson et al. (2020) based on near-glacier kayak surveying and are summarized as follows. In one scenario, the empirical coefficients (turbulent transfer coefficients for heat and salt, Γ_T and Γ_S, and drag coefficient, C_D) were increased until theory could match the observed meltwater intrusions, which required $\sqrt{C_D}\Gamma_{S,T}$ to be 13 times the standard value in the ambient melt regime. In another scenario, an estimate of the realistic horizontal velocity field was incorporated into the theoretical

calculation of ambient melting, which then only required a more modest adjustment to the standard coefficients $\left(4 \times \sqrt{C_D}\Gamma_{S,T}\right)$ in order to match kayak observations.

These two adjusted scenarios for ambient melt, inspired by independent measurements of meltwater intrusions, are combined with standard discharge-driven melt to generate adjusted scenarios for total melt that can be compared with the ocean budgets in Figure 5c. The dashed line illustrates the scenario with enhanced coefficients $\left(13 \times \sqrt{C_D}\Gamma_{S,T}\right)$ over the ambient melt regime, while still assuming that the velocity component that drives melt is only from upwelling plumes. In this scenario, the total melt flux (ambient plus discharge-driven) is enhanced by an order of magnitude compared to standard theory, but melt becomes relatively independent of subglacial discharge. The dotted line illustrates the scenario with a quasi-realistic horizontal velocity and smaller adjustments to the coefficients $\left(4 \times \sqrt{C_D}\Gamma_{S,T}\right)$. In order to generate this scenario across a range of discharge conditions, we make one critical assumption that goes beyond the scope of Jackson et al. (2020), which explored only one season: here we assume the horizontal velocity field across the terminus scales linearly with the energy in the upwelling discharge plume ($u_{\text{hor}} \sim w_{\text{dis. plume}}$), and we determine a constant of proportionality using the average along-terminus velocity from September 2018 as reported in Jackson et al. (2020). The physical basis for this approximation is that a more energetic discharge plume—both in its entrainment at depth and near-surface outflow—should generate a more energetic secondary velocity field of eddies, internal waves, recirculations, and other modes of velocity that could enhance ambient melt. This is speculative, but it presents a physically plausible scenario that could explain how the total melt retains the $Q_R^{1/3}$ scaling when ambient melt is a significant contributor to the total melt flux.

This second scenario is closest to the budget observations (Figure 5c), in both the magnitude and the relationship between subglacial discharge and submarine melt. While these adjustments to theory are speculative, it is notable that the "best guess" adjustment to theory, proposed on the basis of independent kayak surveying in Jackson et al. (2020), creates a theoretical curve that falls relatively close to the budget-derived fluxes. Furthermore, the discrepancy between the kayak-based adjusted theory and the empirical best fit (dotted vs. solid gray in Figure 5c) could be closed with only a modest additional adjustment to theory: either increasing the coefficients by $5.5 \times \sqrt{C_D}\Gamma_{S,T}$ (instead of $4 \times \sqrt{C_D}\Gamma_{S,T}$) or increasing the scale factor between u_{hor} and $w_{\text{dis.plume}}$ by 38%. These are relatively small adjustments compared to the uncertainties involved in tuning theory with kayak-based observations.

5.3.2. Toward an Updated Representation of Melt in Ocean-Glacier Models

Ocean-glacier models require bulk parameterizations for the relationship between submarine melt and its forcing parameters, such as subglacial discharge and fjord temperature (e.g., Slater et al., 2020). This study presents one of the first observational attempts at testing the form of this relationship. However, the empirical fit to the data here should not be applied indiscriminately to other tidewater glaciers without further investigation. To generate a parameterization for tidewater glaciers that is generalizable, physics-based, and observationally validated, further progress is needed in the following areas.

First, we need a better understanding of what drives the near-ice velocity across the whole terminus. While upwelling plumes have received the most attention, the other processes that can drive near-ice velocity—eddies and recirculations, internal waves, calving events, etc. (Kienholz et al., 2019; MacAyeal et al., 2011; Slater et al., 2018)—are poorly understood and rarely observed in situ. Thus we lack a generalizable theory for the terminus-wide ocean velocity field, which is required to predict submarine melting. In the previous section, we speculated that the average terminus-wide velocity might scale linearly with the upwelling velocity of the subglacial discharge plume—a hypothesis that is consistent with the data—but further investigation of the 3D circulation near tidewater termini is needed.

Second, the relationship between the near-ice velocity and submarine melt, as commonly represented by the three-equation melt parameterization (Holland & Jenkins, 1999), is untested at tidewater glaciers. The standard set of coefficients (Cowton et al., 2015; Jenkins, 2011) are derived from studies of ice shelves and sea ice, that is, near-horizontal ice boundaries where the dynamics and morphology might be substantially different.

Furthermore, the functional form of the three-equation parameterization, which assumes a shear-driven boundary layer, is questionable in low-velocity conditions (McConnochie & Kerr, 2017).

Finally, while our results explore the scaling between melt and subglacial discharge, the data does not provide sufficient constraints on the scaling between melt and ocean temperature or stratification, which is needed for a complete melt parameterization.

5.4. Links Between Submarine Melt and Glacier Dynamics

We find the submarine melt flux to be 46%–49% of the total ice flux in three summer surveys, with this percentage dropping to 33% in May (Table 2). While these survey results are the most robust comparison between oceanic and glacier fluxes, in Section 4.5 (Figure 8) we extrapolated to seasonal timescales to explore the effect of submarine melt on terminus stability, calving, and upstream glacier dynamics.

Submarine melt, as modeled based on the empirical results of the oceanic budgets, is primarily controlled by subglacial discharge. Melt peaks during the summers, accounting for ∼50% of the ice flux into the terminus and ∼40% total ablation, and then becomes almost negligible to the terminus budget in winter. During the winter, calving becomes the dominant ablation mechanism. The changes in Q_M are anticorrelated with glacier volume change, with retreat during summer switching to advance in late fall and early winter.

In contrast to trends exhibited by Q_M, Q_{calv} (as well as Q_{glac} and Q_{abl}) continues to increase into late fall 2016 before declining during winter months. With the glacier retreating into deeper water and a reverse slope during the summer (figure 2 in Eidam et al., 2020), the terminus would become more buoyant, unstable, and prone to calving. Terminus velocity usually increases with the reduction in back-pressure, resulting in thinning caused by extensional strain, which, combined with seasonal surface ablation, further increases buoyancy and thus calving (e.g., Pfeffer, 2007).

Calving flux dramatically dropped during the winter months, reaching a minimum in late March 2017. This drop in Q_{calv} and slowdown in Q_{glac} coincide with the presence of ice mélange from March to mid-April, 2017 (Amundson et al., 2020). Ice mélange transmits resistive stresses to the terminus, inhibiting calving, slowing the glacier, and allowing the terminus to advance (Burton et al., 2018). At LeConte, breakup of the ice mélange in 2017 coincided with increases in Q_R (Amundson et al., 2020) and consequently in modeled Q_M. The presence of ice mélange likely inhibited the onset of seasonal retreat when compared to 2016.

We cannot robustly evaluate the correlation between melt and calving because these time series are not independent (Equation 7); however, we note the absence of a strong positive correlation between melt and calving. While this is contrary to the hypothesis that melt enhances calving (e.g., Benn et al., 2017; O'Leary & Christoffersen, 2013), others (e.g., Ma & Bassis, 2019; Slater et al., 2021) argue that the effects of submarine melt on calving can be wide ranging, depending on the profile and magnitude of melt, and in some cases can inhibit calving. For summer conditions at LeConte Glacier, when Q_M is relatively large compared to ice flux, the Ma and Bassis (2019) model suggests a reduction in iceberg size and quantity, with icebergs mainly generated by collapse of the subaerial undercut face. Their results align with observations made by Motyka et al. (2003); Kienholz et al. (2019) at LeConte Glacier, and by Bartholomaus et al. (2013) at Yahtse Glacier.

In summary, the time series analysis suggests that, during summer months, submarine melting is the principal driver of terminus position, leading to seasonal retreat. In winter 2017, when submarine melt is small, glacier dynamics become the principal driver, with calving as the dominant mechanism for frontal ablation. In this winter regime, we posit that the glacier adjusts to a certain terminus position independently of submarine melt, and the evolution of the glacier is mainly driven by the internal dynamics of ice flow, subglacial topography, and channel geometry as well as the presence (or absence) of ice mélange (Truffer & Motyka, 2016).

6. Conclusions

With fjord transects of velocity, temperature, and salinity, we have made 45 estimates of the freshwater fluxes from LeConte Glacier across spring, summer and early fall conditions. We find that the subglacial discharge fluxes inferred from fjord budgets are in relatively good agreement with an independent SMB model for glacier runoff. Submarine melt estimates from the budgets are similar in magnitude to other melt estimates from

multibeam sonar and kayak surveying (Jackson et al., 2020; Sutherland et al., 2019), though slightly higher than the multibeam-derived estimates.

Examining the relationship between submarine melt and subglacial discharge, we find that the observations follow the scaling predicted by standard plume-melt theory, $Q_M \sim Q_R^{1/3}$ (Jenkins, 2011; Slater et al., 2016), but the total submarine melt flux is an order of magnitude higher than predicted when theory is applied with the common set of empirical coefficients. Previous work has shown that ambient melt is a significant part of the total terminus ablation (Jackson et al., 2020). Although ambient melt is not directly driven by subglacial discharge, our results here suggest that ambient melt might still scale with discharge, for example, if the discharge plume energizes the velocity field across the terminus. Across the range of conditions observed, subglacial discharge is the dominant control on melt variability. Fjord conditions (temperature and stratification) have a smaller influence, and the nature of the relationship between melt and fjord conditions is not discernible in the data set. This analysis presents the first attempt at observationally testing the theoretical relationship between melt and discharge across a wide range of subglacial discharge conditions, which is a necessary step toward an accurate parameterizations of submarine melt in ocean-glacier models at a variety of scales.

Comparing the oceanic fluxes with glacier records, we find that submarine melt accounts for one third to one half of the ice flux into the terminus during spring, summer and early fall conditions. Extrapolating to seasonal time series, we find that modeled submarine melt correlates well with terminus position and accounts for up to 40% of frontal ablation during summer periods. Interestingly, submarine melt does not appear to directly increase the calving flux, but it may indirectly affect calving by causing the terminus to retreat into deeper water, thus promoting tidewater glacier instability.

Data Availability Statement

The oceanographic data (CTD and ADCP) are archived with the National Centers for Environmental Information (Accession 0189574, https://accession.nodc.noaa.gov/0189574), and the glacier data are archived at the Arctic Data Center (https://doi.org/10.18739/A22G44).

References

Amundson, J. M., Kienholz, C., Hager, A. O., Jackson, R. H., Motyka, R. J., Nash, J. D., & Sutherland, D. A. (2020). Formation, flow and break-up of ephemeral ice mélange at LeConte Glacier and Bay, Alaska. *Journal of Glaciology*, 66(258), 577–590. https://doi.org/10.1017/jog.2020.29

Bartholomaus, T. C., Larsen, C. F., & O'Neel, S. (2013). Does calving matter? Evidence for significant submarine melt. *Earth and Planetary Science Letters*, 380, 21–30. https://doi.org/10.1016/j.epsl.2013.08.014

Bartholomaus, T. C., Stearns, L. A., Sutherland, D. A., Shroyer, E. L., Nash, J. D., Walker, R. T., et al. (2016). Contrasts in the response of adjacent fjords and glaciers to ice-sheet surface melt in West Greenland. *Annals of Glaciology*, 57(73), 25–38. https://doi.org/10.1017/aog.2016.19

Benn, D., Astrom, J., Zwinger, T., Todd, J., Nick, F., Cook, S., et al. (2017). Melt-under-cutting and buoyancy-driven calving from tidewater glaciers: New insights from discrete element and continuum model simulations. *Journal of Glaciology*, 63, 1–702. https://doi.org/10.1017/jog.2017.41

Burton, J. C., Amundson, J. M., Cassotto, R., Kuo, C.-C., & Dennin, M. (2018). Quantifying flow and stress in ice mélange, the world's largest granular material. *Proceedings of the National Academy of Sciences*, 115(20), 5105–5110. https://doi.org/10.1073/pnas.1715136115

Carroll, D., Sutherland, D., Hudson, B., Moon, T., Catania, G. A., Shroyer, E. L., et al. (2016). The impact of glacier geometry on meltwater plume structure and submarine melt in Greenland fjords. *Geophysical Research Letters*, 43, 9739–9748. https://doi.org/10.1002/2016gl070170

Carroll, D., Sutherland, D. A., Shroyer, E. L., Nash, J. D., Catania, G. A., & Stearns, L. A. (2015). Modeling turbulent subglacial meltwater plumes: Implications for fjord-scale buoyancy-driven circulation. *Journal of Physical Oceanography*, 45(8), 2169–2185. https://doi.org/10.1175/jpo-d-15-0033.1

Cenedese, C., & Gatto, V. M. (2016). Impact of a localized source of subglacial discharge on the heat flux and submarine melting of a Tidewater glacier: A laboratory study. *Journal of Physical Oceanography*, 46(10), 3155–3163. https://doi.org/10.1175/jpo-d-16-0123.1

Cowton, T., Slater, D., Sole, A., Goldberg, D., & Nienow, P. (2015). Modeling the impact of glacial runoff on fjord circulation and submarine melt rate using a new subgrid-scale parameterization for glacial plumes. *Journal of Geophysical Research: Oceans*, 120, 796–812. https://doi.org/10.1002/2014jc010324

De Andrés, E., Slater, D. A., Straneo, F., Otero, J., Das, S., & Navarro, F. (2020). Surface emergence of glacial plumes determined by fjord stratification. *The Cryosphere*, 14(6), 1951–1969. https://doi.org/10.5194/tc-14-1951-2020

Eidam, E. F., Sutherland, D., Duncan, D., Kienholtz, C., Amundson, J. M., & Motyka, R. (2020). Morainal Bank evolution and impact on terminus dynamics during a Tidewater glacier stillstand. *Journal of Geophysical Research: Earth Surface*, 125(11), 119–120. https://doi.org/10.1029/2019jf005359

Hager, A. O., Sutherland, D. A., Amundson, J. M., Jackson, R. H., Kienholz, C., Motyka, R. J., & Nash, J. D. (2022). Subglacial discharge reflux and buoyancy forcing drive seasonality in a silled glacial fjord. *Journal of Geophysical Research: Oceans*, 127(5), e2021JC018355. https://doi.org/10.1029/2021jc018355

Heuzé, C., Wåhlin, A., Johnson, H. L., & Münchow, A. (2017). Pathways of meltwater export from Petermann Glacier, Greenland. *Journal of Physical Oceanography*, 47(2), 405–418. https://doi.org/10.1175/jpo-d-16-0161.1

Hock, R. (1999). A distributed temperature-index ice- and snowmelt model including potential direct solar radiation. *Journal of Glaciology*, *45*(149), 101–111. https://doi.org/10.3189/S0022143000003087

Hock, R. (2005). Glacier melt: A review of processes and their modelling. *Progress in Physical Geography: Earth and Environment*, *29*(3), 362–391. https://doi.org/10.1191/0309133305pp453ra

Hock, R., & Noetzli, C. (1997). Areal melt and discharge modelling of Storglaciären, Sweden. *Annals of Glaciology*, *24*, 211–216. https://doi.org/10.3189/S0260305500012192

Holland, D. M., & Jenkins, A. (1999). Modeling thermodynamic ice-ocean interactions at the base of an ice shelf. *Journal of Physical Oceanography*, *29*(8), 1787–1800. https://doi.org/10.1175/1520-0485(1999)029<1787:mtioia>2.0.co;2

Inall, M. E., Murray, T., Cottier, F. R., Scharrer, K., Boyd, T. J., Heywood, K. J., & Bevan, S. L. (2014). Oceanic heat delivery via Kangerdlugssuaq Fjord to the south-east Greenland ice sheet. *Journal of Geophysical Research: Oceans*, *119*, 1–15. https://doi.org/10.1002/2013jc009295

Jackson, R. H., Nash, J. D., Kienholtz, C., Sutherland, D., Amundson, J. M., Motyka, R., et al. (2020). Meltwater intrusions reveal mechanisms for rapid submarine melt at a Tidewater glacier. *Geophysical Research Letters*, *47*(2), 1–10. https://doi.org/10.1029/2019gl085335

Jackson, R. H., Shroyer, E. L., Nash, J. D., Sutherland, D., Carroll, D., Fried, M. J., et al. (2017). Near-glacier surveying of a subglacial discharge plume: Implications for plume parameterizations. *Geophysical Research Letters*, *39*(73), 25–29. https://doi.org/10.1002/2017GL073602

Jackson, R. H., & Straneo, F. (2016). Heat, salt, and freshwater budgets for a glacial fjord in Greenland. *Journal of Physical Oceanography*, *46*(9), 2735–2768. https://doi.org/10.1175/JPO-D-15-0134.1

Jenkins, A. (2011). Convection-driven melting near the grounding lines of ice shelves and tidewater glaciers. *Journal of Physical Oceanography*, *41*(12), 2279–2294. https://doi.org/10.1175/jpo-d-11-03.1

Jenkins, A., Nicholls, K. W., & Corr, H. F. J. (2010). Observation and parameterization of ablation at the base of Ronne Ice Shelf, Antarctica. *Journal of Physical Oceanography*, *40*(10), 2298–2312. https://doi.org/10.1175/2010jpo4317.1

Johnson, H. L., Münchow, A., Falkner, K. K., & Melling, H. (2011). Ocean circulation and properties in Petermann Fjord, Greenland. *Journal of Geophysical Research*, *116*(C1), C01003. https://doi.org/10.1029/2010jc006519

Kienholz, C., Amundson, J. M., Motyka, R. J., Jackson, R. H., Mickett, J. B., Sutherland, D. A., et al. (2019). Tracking icebergs with time-lapse photography and sparse optical flow, LeConte Bay, Alaska, 2016–2017. *Journal of Glaciology*, *11*, 1–17. https://doi.org/10.1017/jog.2018.105

Lerczak, J. A., Geyer, W. R., & Chant, R. (2006). Mechanisms driving the time-dependent salt flux in a partially stratified estuary. *Journal of Physical Oceanography*, *36*, 2296–2311. https://doi.org/10.1175/jpo2959.1

Ma, Y., & Bassis, J. N. (2019). The effect of submarine melting on calving from marine terminating glaciers. *Journal of Geophysical Research: Earth Surface*, *3*(100), 9–13. https://doi.org/10.1029/2018jf004820

MacAyeal, D. R. (1985). Evolution of tidally triggered meltwater plumes below ice shelves. In *Oceanology of the Antarctic continental shelf* (pp. 133–143). Publisher: American Geophysical Union. https://doi.org/10.1029/ar043p0133

MacAyeal, D. R., Abbot, D. S., & Sergienko, O. V. (2011). Iceberg-capsize tsunamigenesis. *Annals of Glaciology*, *52*(58), 51–56. https://doi.org/10.3189/172756411797252103

Magorrian, S. J., & Wells, A. J. (2016). Turbulent plumes from a glacier terminus melting in a stratified ocean. *Journal of Geophysical Research: Oceans*, *121*, 1–27. https://doi.org/10.1002/2015jc011160

Mankoff, K. D., Straneo, F., CenedeseDas, S. B., Richards, C. G., Singh, H., & Singh, H. (2016). Structure and dynamics of a subglacial discharge plume in a Greenlandic fjord. *Journal of Geophysical Research: Oceans*, *121*(12), 8670–8688. https://doi.org/10.1002/2016jc011764

McConnochie, C. D., & Kerr, R. C. (2017). Testing a common ice-ocean parameterization with laboratory experiments. *Journal of Geophysical Research: Oceans*, *122*(7), 5905–5915. https://doi.org/10.1002/2017jc012918

McNabb, R. W., Hock, R., & Huss, M. (2015). Variations in Alaska tidewater glacier frontal ablation, 1985–2013. *Journal of Geophysical Research: Earth Surface*, *120*(1), 120–136. https://doi.org/10.1002/2014jf003276

Moffat, C., Tapia, F. J., Nittrouer, C. A., Hallet, B., Bown, F., Boldt Love, K., & Iturra, C. (2018). Seasonal evolution of ocean heat supply and freshwater discharge from a rapidly retreating Tidewater glacier: Jorge Montt, Patagonia. *Journal of Geophysical Research: Oceans*, *123*(6), 4200–4223. https://doi.org/10.1002/2017jc013069

Motyka, R. J., Dryer, W. P., Amundson, J., Truffer, M., & Fahnestock, M. (2013). Rapid submarine melting driven by subglacial discharge, LeConte Glacier, Alaska. *Geophysical Research Letters*, *40*(19), 5153–5158. https://doi.org/10.1002/grl.51011

Motyka, R. J., Hunter, L., Echelmeyer, K., & Connor, C. (2003). Submarine melting at the terminus of a temperate tidewater glacier, LeConte Glacier, Alaska, USA. *Annals of Glaciology*, *36*, 57–65. https://doi.org/10.3189/172756403781816374

Motyka, R. J., Truffer, M., Fahnestock, M., Mortensen, J., Rysgaard, S., & Howat, I. (2011). Submarine melting of the 1985 Jakobshavn Isbræ floating tongue and the triggering of the current retreat. *Journal of Geophysical Research*, *116*(F1). https://doi.org/10.1029/2009jf001632

Nick, F. M., Vieli, A., Howat, I. M., & Joughin, I. (2009). Large-scale changes in Greenland outlet glacier dynamics triggered at the terminus. *Nature Geoscience*, *2*(2), 110–114. https://doi.org/10.1038/ngeo394

O'Leary, M., & Christoffersen, P. (2013). Calving on tidewater glaciers amplified by submarine frontal melting. *The Cryosphere*, *7*(1), 119–128. https://doi.org/10.5194/tc-7-119-2013

Pfeffer, W. T. (2007). A simple mechanism for irreversible tidewater glacier retreat. *Journal of Geophysical Research: Earth Surface*, *112*(F3). https://doi.org/10.1029/2006jf000590

Rignot, E., Koppes, M., & Velicogna, I. (2010). Rapid submarine melting of the calving faces of West Greenland glaciers. *Nature Geoscience*, *3*(3), 187–191. https://doi.org/10.1038/ngeo765

Schaffer, J., Kanzow, T., von Appen, W.-J., von Albedyll, L., Arndt, J. E., & Roberts, D. H. (2020). Bathymetry constrains ocean heat supply to Greenland's largest glacier tongue. *Nature Geoscience*, *13*(3), 227–231. Retrieved from https://www.nature.com/articles/s41561-019-0529-x https://doi.org/10.1038/s41561-019-0529-x

Sciascia, R., Straneo, F., Cenedese, C., & Heimbach, P. (2013). Seasonal variability of submarine melt rate and circulation in an East Greenland fjord. *Journal of Geophysical Research: Oceans*, *118*(5), 2492–2506. https://doi.org/10.1002/jgrc.20142

Slater, D. A., Benn, D. I., Cowton, T. R., Bassis, J. N., & Todd, J. A. (2021). Calving multiplier effect controlled by melt undercut geometry. *Journal of Geophysical Research: Earth Surface*, *126*(7), e2021JF006191. https://doi.org/10.1029/2021jf006191

Slater, D. A., Felikson, D., Straneo, F., Goelzer, H., Little, C. M., Morlighem, M., et al. (2020). Twenty-first century ocean forcing of the Greenland ice sheet for modelling of sea level contribution. *The Cryosphere*, *14*(3), 985–1008. https://doi.org/10.5194/tc-14-985-2020

Slater, D. A., Goldberg, D. N., Nienow, P. W., & Cowton, T. R. (2016). Scalings for submarine melting at tidewater glaciers from buoyant plume theory. *Journal of Physical Oceanography*, *46*, 1839–1855. https://doi.org/10.1175/jpo-d-15-0132.1

Slater, D. A., Nienow, P. W., Cowton, T. R., Goldberg, D. N., & Sole, A. J. (2015). Effect of near-terminus subglacial hydrology on tidewater glacier submarine melt rates. *Geophysical Research Letters*, *42*, 2861–2868. https://doi.org/10.1002/2014gl062494

Slater, D. A., Straneo, F., Das, S. B., Richards, C. G., Wagner, T. J. W., & Nienow, P. W. (2018). Localized plumes drive front-wide ocean melting of A Greenlandic Tidewater glacier. *Geophysical Research Letters*, *45*(22), 12350–12358. https://doi.org/10.1029/2018gl080763

Slater, D. A., Straneo, F., Felikson, D., Little, C. M., Goelzer, H., Fettweis, X., & Holte, J. (2019). Estimating Greenland tidewater glacier retreat driven by submarine melting. *The Cryosphere*, *13*(9), 2489–2509. https://doi.org/10.5194/tc-13-2489-2019

Straneo, F., & Cenedese, C. (2015). The dynamics of Greenland's glacial fjords and their role in climate. *Annual Review of Marine Science*, *7*(1), 89–112. https://doi.org/10.1146/annurev-marine-010213-135133

Straneo, F., & Heimbach, P. (2013). North Atlantic warming and the retreat of Greenland's outlet glaciers. *Nature*, *504*(7478), 36–43. https://doi.org/10.1038/nature12854

Straneo, F., Sutherland, D. A., Holland, D., Gladish, C., Hamilton, G. S., Johnson, H. L., et al. (2012). Characteristics of ocean waters reaching Greenland's glaciers. *Annals of Glaciology*, *53*(60), 202–210. https://doi.org/10.3189/2012aog60a059

Sutherland, D., Jackson, R. H., Kienholz, C., Amundson, J. M., Dryer, W. P., Duncan, D., et al. (2019). Direct observations of submarine melt and subsurface geometry at a tidewater glacier. *Science*, *365*, 3690–3374. https://doi.org/10.1126/science.aax3528

Truffer, M., & Motyka, R. J. (2016). Where glaciers meet water: Subaqueous melt and its relevance to glaciers in various settings. *Reviews of Geophysics*, *54*(1), 220–239. https://doi.org/10.1002/2015rg000494

Wilson, N., Straneo, F., & Heimbach, P. (2017). Satellite-derived submarine melt rates and mass balance (2011–2015) for Greenland's largest remaining ice tongues. *The Cryosphere*, *11*(6), 2773–2782. https://doi.org/10.5194/tc-11-2773-2017

Wood, M., Rignot, E., Fenty, I., Menemenlis, D., Millan, R., Morlighem, M., et al. (2018). Ocean-induced melt Triggers glacier retreat in northwest Greenland. *Geophysical Research Letters*, *45*(16), 8334–8342. https://doi.org/10.1029/2018gl078024

Xu, Y., Rignot, E., Fenty, I., Menemenlis, D., & Mar Flexas, M. (2013). Subaqueous melting of Store Glacier, West Greenland from three-dimensional, high-resolution numerical modeling and ocean observations. *Geophysical Research Letters*, *40*(17), 1–6. https://doi.org/10.1002/grl.50825